# PART II

# Probability Density Function of HF Noise

Chapter 4

# Introduction to HF Noise

WHAT is high frequency (HF) noise? Is it a Gaussian process? These questions are the crux of Part II. Chapter 4 provides a review of literature dealing with HF noise and attempts to answer these questions. The answers are crucial to support the premise that an assumption of Gaussian noise is not generally valid for HF communications and therefore not valid for modulation recognition algorithms for HF signals. In fact, many researchers (Nolan, Doyle, Mackenzie & O'Mahony 2002, Hero III & Hadinejad-Mahram 1998, Wong & Nandi 2001, Goris 1998, Akmouche 1999, Hsue & Soliman 1990, Nandi & Azzouz 1997, Nandi & Azzouz 1998) rely on an assumption that noise is Gaussian for their modulation recognition algorithms to provide reasonable results. Is this a valid assumption? Is it just an assumption of convenience or is it an assumption made without a good understanding of the transmission medium? The latter two questions are interesting, but the former are the focus here.

## 4.1 A Definition of HF Noise

Electromagnetic noise is an overall composite electric and magnetic field, generally radiating from numerous sources, that can reduce the ability to discern a desirable electromagnetic field from the background electromagnetic field. For the discussion in Part II, electromagnetic noise incorporates naturally occurring radiation sources. It does not include interfering or co-channel signals. The adjectives, *man-made* or *environmental*, apply to noise or interference as an electromagnetic field commonly attributed to electrical circuits, made by humans, that carry time-varying currents. These circuits may be made to deliberately radiate, or they may radiate as a side-effect of the circuits performing various functions. Thus there is a distinction between naturally occurring noise and environmental noise and interference.

Natural electromagnetic noise covers the entire electromagnetic spectrum. And, just as environmental noise is frequency dependent, so is the natural electromagnetic noise. Part II of the thesis focuses on the natural electromagnetic noise found in the HF band, that is *HF noise*.

Naturally occurring HF noise is composed of two main components: atmospheric noise and galactic noise. Atmospheric noise changes with the time of year and location, and is largely influenced by lightning activity (both local and distant). It is well known that that HF noise is impulsive (CCIR 1986). For example, lightning activity at a distant location can, by various ionospheric modes, contribute to the local HF noise distribution. In fact, the component of noise generated by lightning is directional (Coleman 2006). Galactic noise is produced by cosmic radiators such as the sun and stars. The sun is Earth's closest such radiator, and the sunspot number (*i.e.* the number of dark spots on the sun's surface at any given time) is highly correlated with solar flares that affect the ionosphere. These sources of noise affect HF radio-communications as well as radio-communications in other parts of the electromagnetic spectrum. It is clear then, the HF noise distribution is affected by the time of day, season, geographic location, electromagnetic environment, and state of the ionosphere.

## 4.2 Literature Review

An important issue for the development of any communication system, is an understanding of the communication medium. Traditional telephony uses a wired infrastructure as the medium, whereas radio-communications exploits the electromagnetic spectrum.

The Watterson channel model (Watterson & Coon 1969, Watterson, Juroshek & Bensema 1970) is commonly used to study the effects of the HF channel (*i.e.* the electromagnetic medium for HF radio-communications) on a transmitted signal. Unfortunately, the model is often misused in that it is applied to bandwidths greater than 12 kHz. The Watterson model[5] is intended for channels that have bandwidths of 12 kHz or less, stationarity in time and frequency, negligible delay dispersion, and only a low-ray path[6]. Moreover, the model utilizes a Gaussian distribution for HF noise.

Vogler *et al*. (1988, 1990, 1992) have proposed a wideband channel model (excluding HF noise) that can handle arbitrary bandwidths from 1 kHz to several MHz, ordinary and extraordinary waves in both low- and high-ray paths, channels that are very dispersive (*e.g.* spread-F and transauroral paths), and channels that are non-stationary in either the time or frequency domain. The model channel transfer function consists of a deterministic component (equivalent to a "median" transfer function) and a stochastic component.

The deterministic component specifically models ionospheric electron density, ionospheric reflection coefficient, apparent height of reflection, phase for the low-ray and high-ray of the ordinary and extraordinary waves, delay, and Doppler shift. It also includes a scattering function that allows the ionospheric parameters to change with time.

The stochastic component adds delay dispersion (*i.e.* delay time varies with frequency), Gaussian and non-Gaussian spectra for the taps of the model's tap-gain function, delay spread (*i.e.* the spread in time of a transmitted pulse), and Doppler spread (*i.e.* the

[5]There is some doubt amongst researchers of the validity of the Watterson model for even these applications.

[6]A low-ray path is one in which the arriving signal has an angular elevation with respect to the receive site of less than approximately 30° in the vertical plane. A high-ray path can be considered to be above 30° in the vertical plane.

spread in frequency of Doppler effects). The delay spread and Doppler spread is considered to be caused by specular reflections and scattering from irregularities and refractive index fluctuations of the ionosphere. These parameters are combined in the auto-correlation function of a received signal, which includes a delay amplitude factor that provides a measure of the delay spread of a received pulse, a correlation factor that determines the shape and extent of the Doppler spread (with a Gaussian or exponential form), and a phase function for which the first derivative is the Doppler shift and second derivative is the time rate-of-change of the Doppler shift.

Vogler and Hoffmeyer show that the model, with judicious choice of parameters, agrees well with their measured vertical- and oblique-incidence ionograms (conducted over various long and short paths). However, they acknowledge that a methodology is needed for choosing model parameters such as, median layer heights, layer thickness, and penetration frequencies as a function of geography, time of day, season, and sunspot number. They further note that the model does not include the effects of HF noise—an issue that Lemmon & Behm (1991) address.

Lemmon and Behm propose a model of HF noise plus interference. They begin the development of the model by analyzing noise/interference data, recorded with a wideband receiver, to understand the nature of HF noise plus interference. The data consists of forty-two 1 sec records, each of which, contains 8-bit complex samples—8 bits for the in-phase (I) component and 8-bits for the quadrature (Q) component—from an ADC with a sampling rate of 1.024 MHz. The complex bandwidth covered by each record is 800 kHz.

They consider, in both the time domain and frequency domain, the probability density function (PDF) of: I-samples, voltage envelope (*i.e.* $\sqrt{I^2 + Q^2}$), phase (*i.e.* arctan $\frac{Q}{I}$), and power envelope (*i.e.* $I^2 + Q^2$). They also consider the cumulative distribution function (CDF) of the power envelope and the distribution of the threshold-crossings of the voltage envelope. The results of these distributions infer characteristics of the HF noise plus interference. Lemmon and Behm conclude, and thereby define, HF noise as consisting of three components: a Gaussian component, a sum of sinusoidal interferers, and a sum of filtered delta functions. The Gaussian component is, via the central limit theorem, a result of many independent noise sources (Lyapunov 1901, Laplace 1820, de Moivre 1756). Narrowband interferers (*i.e.* man-made signals) are modelled by the

sum of sinusoidal waves, and if dominant, reduce the effect of the central limit theorem. The sum of filtered delta functions model impulsive noise sources (*e.g.* lightning) observed at baseband.

The subsequent complex noise voltage, $z(t)$, is expressed by

$$z(t) = g(t) + \sum_{k=1}^{N_k} A_k \mathrm{e}^{-j(\Delta\omega_k t + \phi_k)} + \sum_{m=1}^{N_m} B_m \frac{\sin\left[2\pi B(t - t_m)\right]}{t - t_m} \mathrm{e}^{j\omega_o t_m}, \tag{4.1}$$

where $g(t)$ is a complex white-Gaussian noise process with a zero mean, $\Delta\omega_k$ are the baseband frequencies of the sinusoidal interferers around some carrier, $\omega_o$, such that $\Delta\omega_k = \omega_k - \omega_o$, $\phi_k$ are random phases, $B$ is the bandwidth (in units of Hz) of the baseband filter of the receiver, $t_m$ are the arrival times of the filtered impulses, $N_k$ is the number of interferers in the band of interest, and $N_m$ is the number of impulses in the time interval of interest. The factors $A_k$ and $B_m$ represent the respective magnitudes of the narrowband interferers and the impulsive noise sources.

Lemmon and Behm then compute the distributions discussed above on the noise voltage of Eq. (4.1) and compare the results with the distributions of the real data. The comparison of the model with the measured data shows good first-order statistical agreement. In fact, in one noise record, which lacks a Gaussian component and numerous interferers, the PDF of the I-samples is remarkably similar to the measured distribution of HF noise discussed in later chapters.

They continue their characterization of HF noise plus interference by considering 2$^{\text{nd}}$-order statistics of the 42-record data set (Lemmon & Behm 1993). This is carried out by comparing the auto-correlation, pulse-width distribution, and pulse-spacing distribution of the measured noise/interference with the corresponding auto-correlation, pulse-width distribution, and pulse-spacing distribution of the model in Eq. (4.1). The auto-correlation specifies the degree to which the process is correlated at different instants of time, and the pulse-width and pulse-spacing distributions describe the times of arrival of impulses.

The second-order statistics of the model agree, in a general sense, with the second-order statistics of the measured noise/interference. To improve the agreement, Lemmon and Behm suggest two modifications to the model. The first refines the model

by introducing a "bursty" distribution rather than a uniform distribution for the impulsive noise component. The second improvement adds a component for wideband atmospheric noise. Finally, they note that an extensive validation program is needed whereby data is recorded and analyzed at numerous sites around the world and at various times of the year.

The previous discussion highlights relatively modern approaches to the modelling of HF noise. Much early research (Aiya 1962, Hoff & Johnson 1952, Furutsu & Ishida 1961, Yuhara, Ishida & Higashimura 1956, Nakai 1960, Likhter Ya 1956, Foldes 1960) throughout the middle-20$^{th}$ century focuses on the probability distribution of the noise. Clarke's (1962) work in England and Ibukun's (1964, 1966) experiments in the tropical areas of Africa yield similar results that suggest a peaked distribution, although Ibukun's results show a significantly greater electric field strength for the noise. The larger field strength values in Ibukun's work are not entirely unexpected, as Ibukun's measurements are from an area of high lightning activity. Both researchers use a narrow bandwidth (approximately 350 Hz) at various *spot* frequencies[7] through which they measure the percentage of time the noise level in the bandwidth exceeds a varying threshold. Ibukun (1966) also discusses a variety of proposed lognormal functions to model HF atmospheric noise. One such model is similar to the model discussed in a later chapter.

## 4.3 Summary

Understanding the nature of the HF channel requires understanding the ionosphere, electromagnetic propagation, noise, and interference and, despite the approximately 100 years of radio-communications research, man's knowledge of these areas is still incomplete. The foregoing review, though not an exhaustive one, highlights some of the unknowns for HF communications.

In particular, it is clear that *HF noise* has various definitions. Based on these definitions, some (Watterson & Coon 1969, Watterson *et al* 1970) assume it is Gaussian, others (Lemmon & Behm 1991) conclude that it consists of a few components (impulsive noise, Gaussian noise, and discrete interferers), yet others (Clarke 1962, Ibukun 1964,

[7] These *spot* frequencies are 24 kHz, 110 kHz, 135 kHz, 11 MHz, and 20 MHz.

Ibukun 1966, Giesbrecht *et al* 2006) conclude that it is non-Gaussian. The work of Lemmon & Behm (1991), Clarke (1962), and Ibukun (1966) foreshadows results reported in Chapter 7. In fact their work supports these new results.

With a basic understanding of HF noise, we now endeavour to measure the probability-density-function (PDF) of the noise through two unique methods. These methods are presented in the next chapter.

Chapter 5

# Methods for Measuring the PDF of HF Noise

WHAT is the probability density function (PDF) of HF noise? Can it be measured? The premise is that an assumption of Gaussian noise is not generally valid for HF communications. Rather, natural HF noise consists of galactic and atmospheric noise, though environmental (man-made) noise (Johnson *et al* 1997) can dominate in populated locations. Also HF noise is known to be impulsive (CCIR 1986) and directional (Coleman 2006). Galactic noise is produced by cosmic radiators such as the sun and other stars. Atmospheric noise changes with time of year and location, and is largely influenced by lightning activity; while environmental noise is produced by electromagnetic radiating devices (*e.g.* electric machinery, power lines and transformers). This chapter describes two new methods of measuring the PDF of HF noise. The first method, called the *swept-narrowband* method, utilizes data from a frequency-sweeping receiver. The second method, aptly named the *broadband* method, stares at a broad band for the entire measurement period.

## 5.1 Introduction to Methods

There are many ways to measure HF radio noise (Clarke 1962, Ibukun 1964, Ibukun 1966, Watterson & Coon 1969, Watterson *et al* 1970, Lemmon & Behm 1991, Lemmon & Behm 1993). However, the methods presented in the following sections are constrained by the form of the data provided by the measuring equipment and less so from inherent limitations of the receiving equipment. The methods, designed after collection of the source data, are therefore not improvements of or replacements for methods designed by other researchers.

Rather, the methods attempt to compute the PDF of natural HF noise from the collected data (see Appendix B). That data is produced using two similar receiving systems (see Chapter 6), a swept-narrowband receiver and a broadband receiver, even though the characteristics of the data produced by these two receivers are sufficiently different to warrant a variation on a common analysis concept.

The premise for each method is that during the sunrise period, the HF noise is dominated by galactic and atmospheric noise. Environmental noise (or man-made noise) levels are comparatively small but, increase throughout the day in line with human activity, and propagate from distant and local sources. Excision of man-made noise is based on a thresholding technique that assumes that the amplitude of atmospheric noise is below the threshold, and the amplitude of man-made noise is above the threshold. Removal of environmental noise from the data set leaves a residue of data suitable for the calculation of the PDF of natural HF noise.

## 5.2 Swept-Narrowband Method

The swept-narrowband method requires data that is swept in time and frequency. This means that each successive sample occurs a time interval, $\Delta T$, after the previous sample. It also means that each successive sample is at a frequency, $\Delta f$ above the previous sample. Such a data set is available from the output of a pre-emptive null-steering ionosonde (Brine, Lim, Massie & Marwood 2002). This ionosonde is used for purposes entirely different from the present investigation and therefore will not be discussed further. However, the ionosonde does provide the raw output of a digital receiver that

is swept across the HF band every 15 minutes. It is this output that forms the basis for the present work.

The receive site is at a location in Adelaide, Australia where there is a relatively high environmental HF noise level. Sweeps are made over a 48-hour time span (February 16–17, 2005) at this site and only data sets created shortly before sunrise[8] and shortly after sunrise are considered. At sunrise the D-region in the ionosphere begins to form and to absorb distant environmental and natural noise propagating by ionospheric modes. Furthermore, the level of local environmental noise is relatively low because people are still asleep but, as people wake and attend to their daily activities the local environmental noise increases significantly. The "best" estimation of the distribution of the natural HF noise is therefore during the sunrise period.

Each sweep covers the 2–25 MHz band at a sweep rate, $F_{\text{swp}} = 125$ kHz/s, and sampling rate[9], $F_{\text{s}} \approx 10$ kHz. The bandwidth covered by the sweep at each sampling instant is denoted by

$$\Delta f = \frac{F_{\text{swp}}}{F_{\text{s}}}. \tag{5.1}$$

The number of samples in a given bandwidth, BW, is therefore

$$N_{\text{samp}} = \frac{\text{BW}}{\Delta f}. \tag{5.2}$$

Every 15 min a sweep covers the 2–25 MHz band in 184 s and contains exactly $\frac{69}{36} \times 10^6$ samples. Each sample is $\Delta f = 12$ Hz higher than the previous sample and is $\Delta T = 96$ $\mu$s later than at the previous sample. Consequently, the sweep only represents a brief 3 min window of the HF band every 15 min. This is less than ideal, as a longer observation time would provide a more complete picture of the noise PDF. Of course, the method is not dependent on the observation time, nor is the observation time dependent on the method. Rather, the observation time in this instance is constrained for reasons unrelated to this work, but related to Brine *et al*'s (2002) research. Nevertheless, the brief window does yield a better understanding of HF noise.

The data from each digital downconverter (DDC) sweep is segmented into bands, BW, (see Figure 5.1) within which the noise statistics are assumed stationary in the wide

[8] On February 17, 2005 sunrise was at 6:51 am in Adelaide, Australia.

[9] The exact sampling rate is $\frac{31250}{3}$ Hz

sense. Within BW, $M$ sub-channels of bandwidth, $\mathrm{BW_c}$, are chosen such that

$$M = \frac{\mathrm{BW}}{\mathrm{BW_c}} \tag{5.3}$$

and where the number of samples in each sub-channel are

$$L = \frac{\mathrm{BW_c}}{f_\mathrm{n}}. \tag{5.4}$$

Typical values for BW, $\mathrm{BW_c}$, and $N_\mathrm{samp}$ are $\approx$ 200 kHz, $\approx$ 1 kHz, and $\approx$ 16000 respectively.

The $90^{\mathrm{th}}$ percentile of the absolute value of the samples in a sub-channel is taken as a the combined amplitude of all HF signals in the sub-channel. This calculation is performed for each sub-channel to form a list of amplitudes. Those sub-channels whose

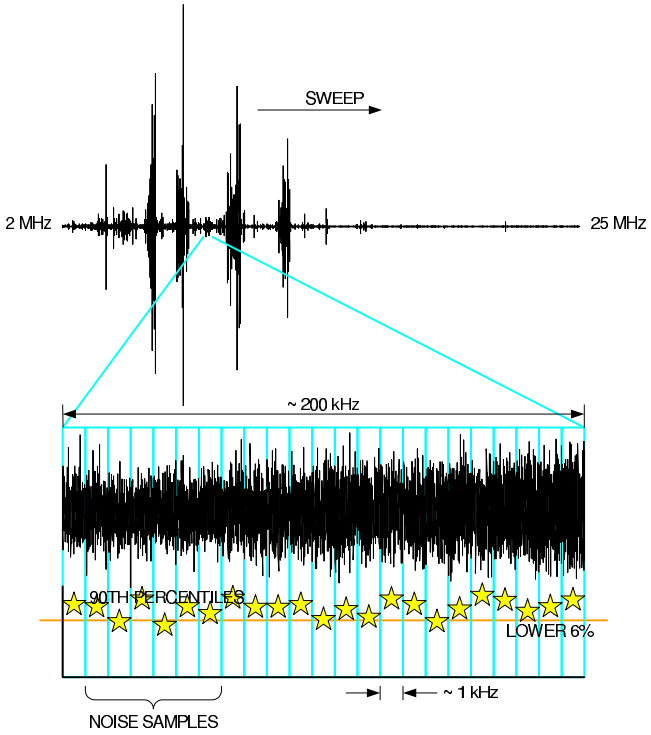


**Figure 5.1. Time-based measurement of HF noise PDF.** The method of determining noise samples requires a sweep in time and frequency across much of the HF band. Data collected from the sweep is sub-divided into $\approx$ 200 kHz bands and further sub-divided into $\approx$ 1 kHz bands. The 1 kHz bands having the lowest $90^{\mathrm{th}}$ percentiles are those that are used in the computation of the PDF for HF noise.

amplitudes are below an $L_p$ percent threshold[10] (in this case 6%) are chosen as sub-channels free of environmental noise. All the time-series samples corresponding to these choice sub-channels are considered noise samples. It is assumed, that normalizing the histogram (100 amplitude bins) of these samples by the number of samples for all chosen sub-channels yields the PDF of the of HF noise. Then, by mapping each sample to a voltage at the output of the antenna and accounting for the antenna factor (see Section 5.4), the noise probability can be plotted as a function of electric field strength. This mapping incorporates the dominant gains and losses in the receiver.

## 5.3 Broadband Method

The broadband method relies on data that is not swept in frequency. In fact, it depends on the broadband receiver being fixed on a particular broad frequency band. Nevertheless, processing of data is similar to that of the swept-narrowband method. The procedure is to

**i)** read in samples of wideband time series (with sample rate, $f_s$);

**ii)** compute the normalized FFT with a bin resolution of $\Delta f$;

**iii)** compute the $N^{\text{th}}$ percentile of each sub-band of bandwidth, $\text{BW}_c$;

**iv)** identify all sub-bands whose $N^{\text{th}}$ percentile falls in the lowest $L_P$ percent of all $N^{\text{th}}$ percentiles;

**v)** "zero-out" all other sub-bands not identified in the previous step;

**vi)** compute the inverse FFT (1 Hz resolution) of the resultant spectrum;

**vii)** compute the histogram (100 amplitude bins) of the real component of the resultant time-series data;

**viii)** convert the samples to electric field strength at the antenna.

[10]The choice of $L_P$ is based on a visual inspection of the frequency domain data and is therefore somewhat arbitrary, but is nevertheless chosen to aid the elimination of bands containing signal energy.

In step ii), $\Delta f = 1$ Hz so that enough frequency-domain samples are present for a statistically significant measure in step iii). Furthermore, $N = 90$ as in the swept-narrowband method, $L_P = 3\%$ as opposed to 6% in the swept-narrowband method[11], and $\mathrm{BW_c}$ is chosen as 1.2 kHz. Scaling of the samples depends on the transducing gain from the antenna to the output of the FFT and by the mapping function in Section 5.4. The transducing gain is discussed in Section 6.3.

Whereas the 3 min datasets resulting from the constraints on the swept-narrowband method provide some understanding of the HF noise, the 30 min observation period for the broadband method should provide a greater understanding. Here too, the observation period is not constrained by the method, nor the method by the observation time. The relatively long viewing time is an arbitrary decision related to the testing of the CTD prototype. It, however, does afford a dataset larger than Brine *et al*'s (2002) dataset and should therefore enable a more accurate measure of the noise PDF.

## 5.4 The Electric Field at each Sampling Instant

Both the swept-narrowband method and the broadband method require a means for converting the digital samples at the output of the process to the equivalent electric field strength at the antenna. Following the approach of the International Telecommunication Union (CCIR 1986), the electric field strength of HF noise can be described by

$$E_\mathrm{n} = F_\mathrm{a} - 95.5 + 20\log_{10}\left(F_\mathrm{MHz}\right) + 10\log_{10}\left(b\right), \tag{5.5}$$

where $E_\mathrm{n}$ is the root-mean-square (RMS) electric field strength of the noise in units of dB with respect to a $\mu$V/m (dB$\mu$V/m) for a bandwidth of $b$ Hz, and where $F_a$ is the effective noise figure (dB) of the antenna at a center frequency of $F_\mathrm{MHz}$ MHz. Moreover, the antenna factor, $f_\mathrm{a}$, is

$$f_\mathrm{a} = \frac{p_\mathrm{n}}{kT_0 b}, \tag{5.6}$$

where $p_\mathrm{n}$ is the noise power (W) available from an equivalent loss-free antenna, $k$ is Boltzmann's constant, and $T_0$ is the reference temperature (288 K as suggested by the

[11] Again, the selection of $L_P$ is based on a visual inspection of the frequency domain data and is chosen to aid the elimination of bands containing signal energy.

ITU). Calculating $10\log_{10}(f_a)$ and inserting into Eq. (5.5) yields

$$E_n = P_n + 20\log_{10}(F_{MHz}) + 108.5, \tag{5.7}$$

where $E_n$ has units of dB$\mu$V/m, and $P_n$ has units of dB with respect to a Watt (dBW). Note that this equation is independent of $b$.

To determine $P_n$, compute $10\log_{10}\left(\frac{y^2[i]}{1\ \Omega}\right) - G$, where $y[i]$ represents the instantaneous sample output from the digital receiver at the $i^{\text{th}}$ sampling instant across an arbitrary impedance[12] of 1 $\Omega$ and where the constant, $G$, accounts for all gains and losses in the receiving system (*i.e.* the transducing gain). This produces an instantaneous noise power, $P_n[i]$, at each sampling instant, $i$. Inserting $P_n[i]$ into Eq. (5.7) yields the instantaneous electric field strength in dB$\mu$V/m,

$$E_n[i] = P_n[i] + 20\log_{10}(F_{MHz}) + 108.5, \tag{5.8}$$

and taking the inverse-logarithm of the result, and accounting for the sign of $y[i]$ renders the instantaneous electric field strength ($\mu$V/m) at each sampling instant across the electronic length of the antenna,

$$e_n[i] = 10^{E_n[i]/20} \times \text{sign}(y[i]), \tag{5.9}$$

where $e_n[i]$ has units of $\mu$V/m.

It must be remembered that $y[i]$ (see Figure 5.2) is an instantaneous value, not an root-mean-square (RMS) value, which is analogous to the instantaneous voltage at the output of an analog receiver. Through the transducing gain, Eq. (5.9) represents the instantaneous electric field strength at the antenna.

[12] In the digital domain impedance is irrelevant, therefore the assumption of an arbitrary impedance for the purposes of the calculation is valid.

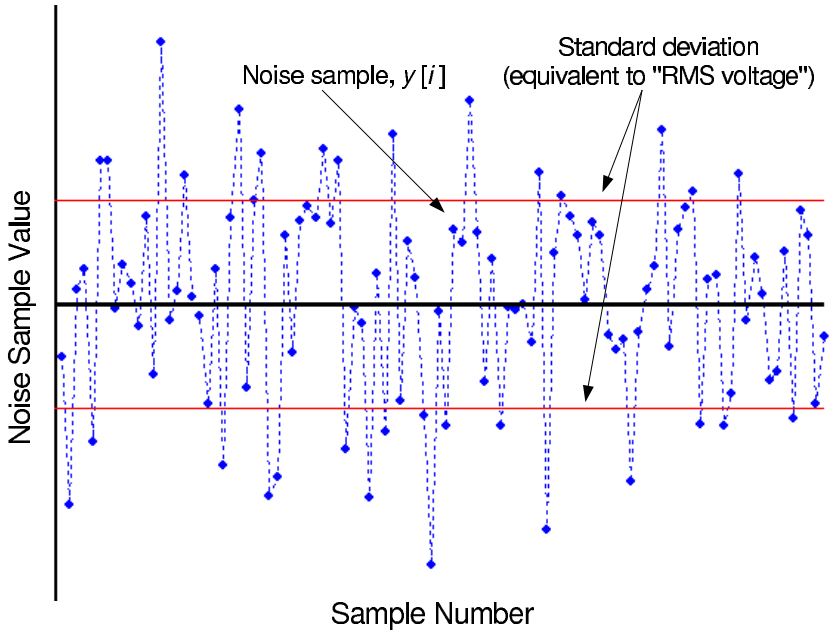


**Figure 5.2. Resulting sequence after excision of environmental noise.** The resulting sequence of digital samples, after excision of environmental noise, is assumed to represent the random variations of electric field strength at the antenna due to natural sources. Each noise sample, which is a base-2 number, can be mapped to a voltage gradient through the transducing gain that accounts for all gains and losses in the receiving system. The square of each sample is the instantaneous power output at the corresponding sampling instant. Referring this to the antenna, converting back to a voltage gradient, and accounting for the sign of the sample, yields the instantaneous electric field strength.

## 5.5 Summary

Two methods of measuring the HF noise PDF are discussed in this chapter. The premise for each method is that during the sunrise period, the HF noise is dominated by galactic and atmospheric noise. The environmental noise component is primarily composed of man-made signals, propagating via skywaves, from distant and local sources.

Both methods attempt to excise environmental noise from the data set and to generate a noise PDF from the residue. The swept-narrowband method requires data recorded from a receiver sweeping in the frequency domain, whereas the broadband method requires data recorded from a receiver that stares at a wide band for the entire measurement period. In both cases, signals with an amplitude above a threshold are removed from the data set. All data samples below the threshold are assumed to be noise samples. The HF noise PDF is generated from these noise samples using simple histogram

techniques. But, how do the receivers acquire the data necessary for the noise analysis? The next chapter answers this question by describing the equipment of each receiver.

Chapter 6

# Experimental Setup for Noise Measurements

EQUIPMENT for the measurement and analysis of HF noise data is described in this chapter. Two different setups are used: one a swept-narrowband receiver and the other a multi-antenna broadband receiver. The swept-narrowband receiver was developed by Brine *et al* (2002) as part of a pre-emptive null-steering ionosonde. Some of its components, namely the ADC, gain control system, and antenna feeders, are the same as those used in the broadband receiver. Furthermore, the description of the swept-narrowband receiver is based on discussions with Brine and is therefore necessarily brief. However, the description of the broadband receiver is as detailed as allowed by its manufacturer (Ebor Computing). The discussion covers system architecture and characteristics, but more importantly, identifies the subset of the broadband receiver in use for data collection.

## 6.1 Receiver Chronology

Three HF receiver systems are discussed in this thesis: two in this chapter, and another in Chapter 11. An awareness of their differences and their developmental chronology is important for a few reasons: 1) it avoids confusion when similar terms and phrases are used in their descriptions; 2) it provides an understanding of limitations and constraints on data sets collected with the receivers; and 3) it helps the reader to link data sets to specific receivers. The second and third points are particularly important to interpret the analysis results provided by the research platform mentioned in Figures 1.1 and 6.4.

An earlier discussion dealt with the definition and purpose of a capability-technology-demonstrator (CTD). The CTD for the broadband receiver covers three stages from 2002 to 2007. The swept-narrowband receiver was developed in parallel with the CTD and has some similarities to the broadband receiver. Figure 6.1 shows the timeframes for the three CTD stages and the swept-narrowband receiver.

The swept-narrowband receiver was developed by Brine *et al* (2002) through the University of Adelaide and with assistance from Ebor Computing. This receiver is designed to aid analysis of ionospheric effects on HF signals; it is described in the next section. A by-product of the data provided by this receiver is that it is useful for the analysis of HF noise.

CTD Stage 1 concluded with an early-prototype HF receiver that had limited bandwidth, eight antennas, two digital receivers, and very basic signal processing capabilities. It was located in an urban industrial estate in Adelaide, Australia. This early prototype was not used for data collection.

The second stage of the CTD improved upon the capabilities of the early-prototype. It added eight antennas (for a total of 16), improved signal processing capabilities, and digital receivers. This developmental receiver is described as the narrowband receiver in Chapter 11; it also was located in an industrial area of Adelaide. Two data collection sessions were conducted with this receiver in December 2003 and another in April 2005. The first session in December 2003 targeted groundwave transmissions of common HF signals under the control of Ebor Computing. The second session in December 2003 targeted high-angle skywave transmissions also under the control of

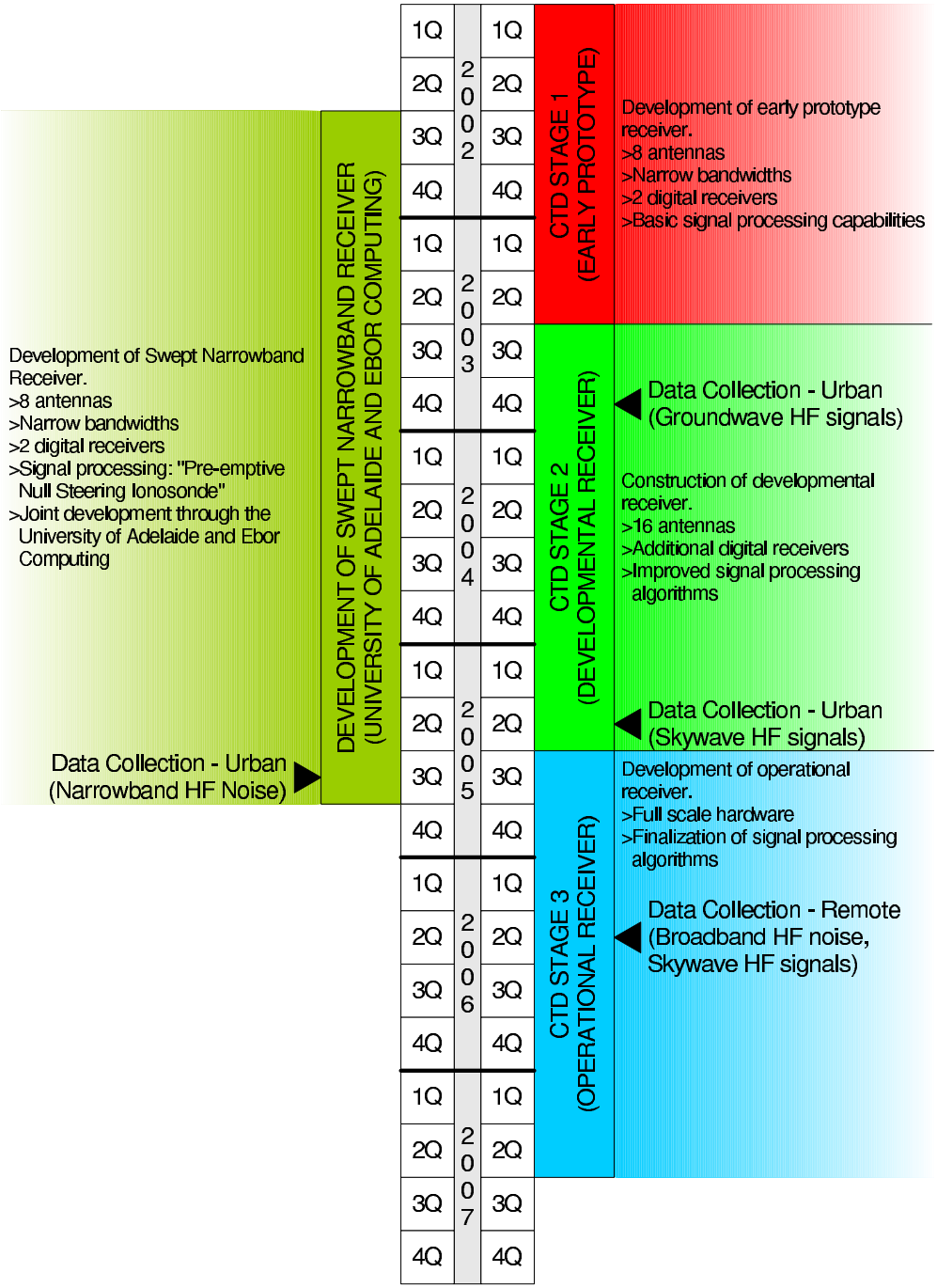


**Figure 6.1. Chronology of receiver development.** A chronology of the development of the broadband receiver and swept-narrowband receiver. Development of the broadband receiver occurred in three stages: an early prototype, a developmental receiver, and an operational receiver. The swept-narrowband receiver was developed in parallel by Brine *et al* (2002) through the University of Adelaide with assistance from Ebor Computing.

Ebor Computing. The last data collection session focussed on signals (both groundwave and skywave) of opportunity out of the control of Ebor Computing. Since the receiver was located in an industrial estate, all the data sets are contaminated with significant environmental noise.

The final stage of the CTD scales-up the developmental receiver to an operational broadband receiver. This receiver has 16 antennas (though it is capable of handling many more), numerous digital receivers to cover the entire HF spectrum, a large bank of computers to perform direction finding, signal enhancement, signal tracking, and characterization of signals. This is the broadband receiver described in Section 6.3. A simplified version of the broadband receiver (see Section 6.3) is used for data collection at a remote site near Swan Reach, South Australia. Two data collection sessions are conducted with this receiver in April 2006 and May 2006. For this thesis, the data is useful in two ways: it provides wideband HF noise information, and it provides known and unknown skywave signals to which the various feature extraction methods (see Part III) can be applied. Swan Reach is far from significant sources of environmental HF noise and so the data sets collected are relatively free of such noise.

## 6.2 Swept-Narrowband Receiver

This section summarizes the receiver described by Brine *et al* (2002), who developed the receiver as part of a pre-emptive null-steering ionosonde. The output of the receiver, however, is useful for the swept-narrowband method of determining the probability density function of HF noise. In this thesis the receiver shall be referred to as the *swept-narrowband* receiver to distinguish it, in a functional sense, from the narrowband receiver and broadband receiver created at Ebor Computing and described in the subsequent sections. The swept-narrowband receiver uses components similar to the other receivers; they include the feeder, gain control system, and ADC. Brine graciously supplied enough information to construct the model in Figure 6.2 for one of the antennas and its associated RF chain.

The actual pre-emptive null-steering ionosonde consists of eight active whip antennas, arranged in an L-shape (see Figure 11.2), that are connected to a custom receiver through a wideband gain control system. This receiver contains eight analog-to-digital

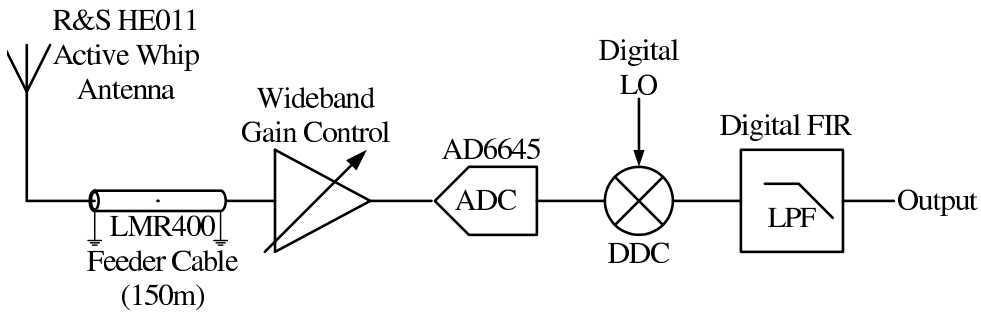


**Figure 6.2. Model of the swept-narrowband receiver.** The swept-narrowband receiver consists of an active whip antenna, feeder, gain control system (see Section 6.3), and digital receiver (ADC, DDC, and FIR filter). The RF chain connected to each of the antennas in the array is shown here.

converters (Analog Devices AD6645) and two digital downconverters (developed at the University of Adelaide). The system described below models one of the eight RF chains.

The HE011 antenna has an antenna factor of 14 dB over the entire HF band. The relationship between antenna factor, $AF$, and antenna gain, $g_a$, is given by

$$AF = 20\log_{10}\left(\frac{9.73}{\lambda\sqrt{g_a}}\right) \tag{6.1}$$

where $\lambda$ is the radio wavelength in meters and $g_a$ is absolute gain of the antenna and $G_a$ is the absolute gain in decibels. The antenna datasheet in Appendix E has more information.

The insertion loss (negative of gain) of the LMR-400 feeder cable is given by the manufacturer (Times Microwave) as

$$L_f = \frac{1250}{381}\left(0.12229\sqrt{F} + 0.00026F\right), \tag{6.2}$$

where $F$ is the frequency in units of MHz and $L_f$ has units of dB/m. Multiplying by the feeder length of 150 m and converting to gain yields a feeder gain of $G_f = -150L_f$ dB and is shown in Figure 6.3.

Gain, $G_{gc}$, and noise figure of the wideband gain control system varies with the configuration of the system. Section 6.3 describes the gain control system in more detail.

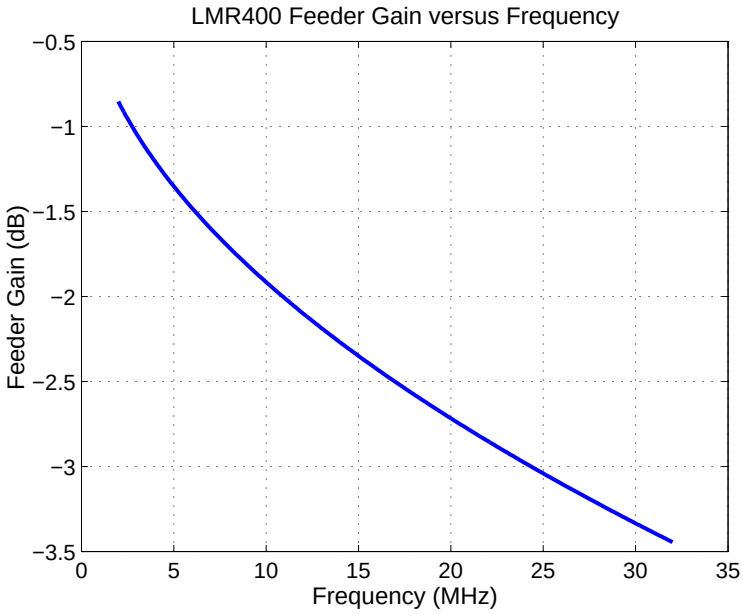


**Figure 6.3. Attenuation of LMR400 coaxial cable.** The antenna feeder consists of a 150 m length of LMR400 coaxial cable. The gain (negative of loss) of this cable type is a function of frequency and cable characteristics. The negative of the loss equation, defined by the manufacturer, is plotted here.

For the swept-narrowband receiver the gain control system is configured to provide a fixed gain of 24 dB.

Finally, for a +4 dBm input to the ADC the output of the digital filter is equivalent to 130 dB relative to an arbitrary impedance (in the digital domain) of 1 Ω. Given that the input impedance of the ADC is 50 Ω, the corresponding voltage[13] at +4 dBm is 354 $\text{mV}_{\text{rms}}$. The 130 dB output corresponds to a voltage $3.16 \times 10^6$ V. The seemingly large voltage[14] is due to processing gain. Samples grow from 14-bits at the output of the ADC to 40-bits at the output of the custom DDC. Consequently the transducing gain from analog input to digital output is $G_{\text{tg}} = 10 \log \left( \frac{3.16 \times 10^6}{0.354\ \text{V}_{\text{rms}}} \right) = 69.5$ dB.

With all of this in mind, the overall gain from antenna input to DDC output is

$$G_{\text{T}} = G_{\text{a}} + G_{\text{f}} + G_{\text{gc}} + G_{\text{tg}}. \tag{6.3}$$

[13]The voltage is computed as $\sqrt{50} \times 10^{\frac{4-30}{20}}$.

[14]The calculation of the voltage is $10^{\frac{130}{20}}$.

This gain varies with frequency and accounts for gain of the analog front-end, the transfer function of the ADC, and the processing gain achieved through the DDC.

The ADC used by the swept-narrowband receiver is the AD6645 from Analog Devices. The AD6645 is capable of sampling signals with a sampling clock up to 105 MHz with 14-bit resolution, though the sampling rate for this setup is 50 MHz. The swept-narrowband receiver also uses multiple custom DDCs. A detailed description of how these customized DDCs operate is not necessary here, except to say that they operate in a manner very similar to the Texas Instruments GC4016 DDC (see Appendix E).

## 6.3 Broadband Receiver

The prototype broadband receiver (see Figure 6.4) consists of an array of antennas, followed by signal conditioning electronics, multiple digital receivers, and a data processing sub-system.

Analog pre-processing conditions the HF signal for processing by the digital receivers. The digital receivers directly sample RF signals up to a frequency of 50 MHz and downconvert wideband or narrowband HF channels to baseband. Wideband analog-to-digital (ADC) converters digitize the RF signals while downconversion is accomplished with digital downconverters (DDCs). After downconversion, a data processing sub-system collects and analyses the baseband information. It performs functions

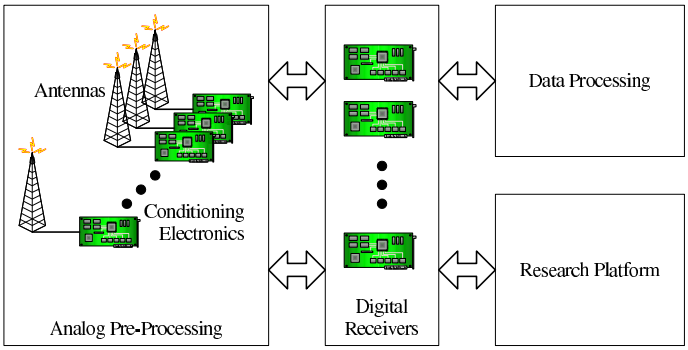


**Figure 6.4. Architecture of the advanced HF receiver (repeated).** Architecture of the prototype receiving system consisting of analog, digital, and data processing sections. The research platform supports the work in Part III of the thesis (Figure 1.1 repeated for convenience).

(hereafter referred to as core functions) such as direction finding (in azimuth and elevation), signal enhancement, signal tracking, and feature extraction. The research platform supports work on modulation recognition algorithms and is discussed later in Part III.

The broadband receiver is scaleable. Antennas plus associated signal conditioning electronics, receiver modules, and processing modules can be added or subtracted from the system to increase or decrease the system's capabilities. For example, there is a one-to-one mapping of antennas (plus signal conditioning) and receiver modules. Every additional antenna and receiver module improves the performance of the core functions in terms of the number of separable signals, accuracy of direction finding, ability to track signals, and the ability to enhance signals. Furthermore, every additional processing module provides additional coverage of the HF band. With enough processing modules, the entire HF band can be processed simultaneously.

## Analog Pre-Processing

Analog pre-processing includes passive antennas and a wideband gain control system. The arrangement of antennas is arbitrary and is chosen based on operational goals. One might choose a circular array to balance inter-element coupling and minimize spatial ambiguities, whereas an L-array or linear array may be used to provide accurate signal directions in a particular hemispherical sector.

The wideband gain control system in Figure 6.5 monitors the average signal energy over the HF band from each antenna. The gain control system limits the bandwidth of the signals to 2 - 32 MHz with 7th order Chebyshev filters. At the output of the filters, a -20 dB coupler allows a small portion of the RF signal to feed a logarithmic amplifier, which drives a power meter and provides the feedforward signal to the gain control algorithm. The meter is used to indicate when the gain should be changed if the gain system is operated in the manual mode. Following the coupler are the variable gain stages with a gain range of -6 dB to +36 dB. Each stage is controlled independently. The noise figure for the gain control system ranges from 1.2 dB to 12.3 dB depending on which gain stages are switched in or out. This can be determined from a cascade

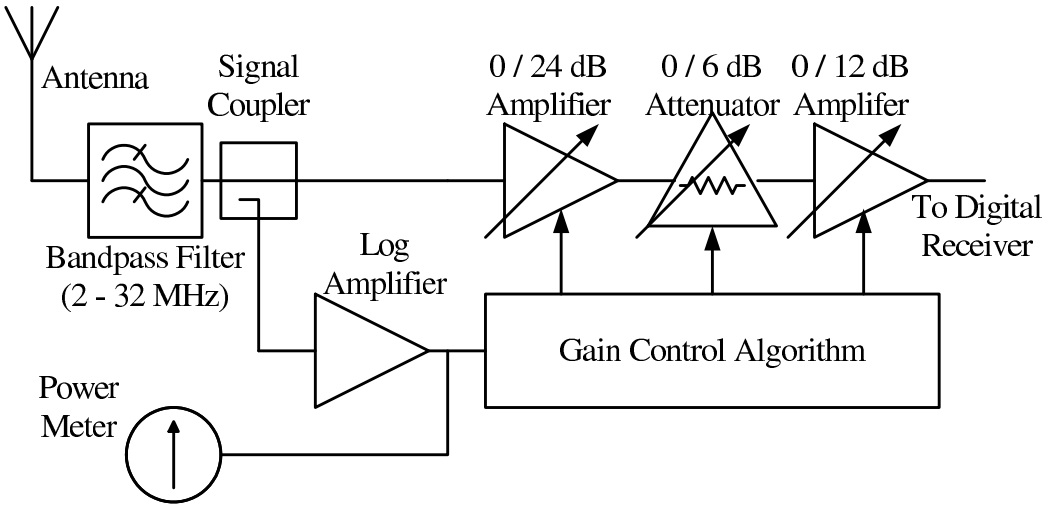


**Figure 6.5. Schematic of wideband gain control system.** The gain control algorithm adjusts the amplifier and attenuator settings based on a measurement of the signal level at the output of the bandpass filter and is applied to the signal provided by each antenna. A simple algorithm adjusts the gain upward or downward depending on the measured energy across the entire HF band.

analysis of the RF chain (see Appendix C). A feedforward gain control algorithm adjusts the gain in response to diurnal, and seasonal changes in the HF environment. Its goal is to maintain the average wideband power level to -20 dBm (over a bandwidth of 28 MHz) at the input to the ADCs. This provides some margin for large signals that appear only momentarily. If necessary, the gain control algorithm will quickly reduce the gain to protect the ADCs from extremely large transient signals in the HF band (*e.g.* sustained lightning activity). The gain can also be adjusted manually.

## Digital Receivers

The ICS554 digital receiver card, available from Radstone-ICS, is the heart of each receiver module (see Figure 6.6). A receiver module consists of one digital receiver and a dual-CPU rackmount (3RU) computer. Signal mixing and downconversion is done on the digital receiver. The computer extracts the downconverted signals from the digital receiver and forwards the data to the processing modules over a giga-bit ethernet network.

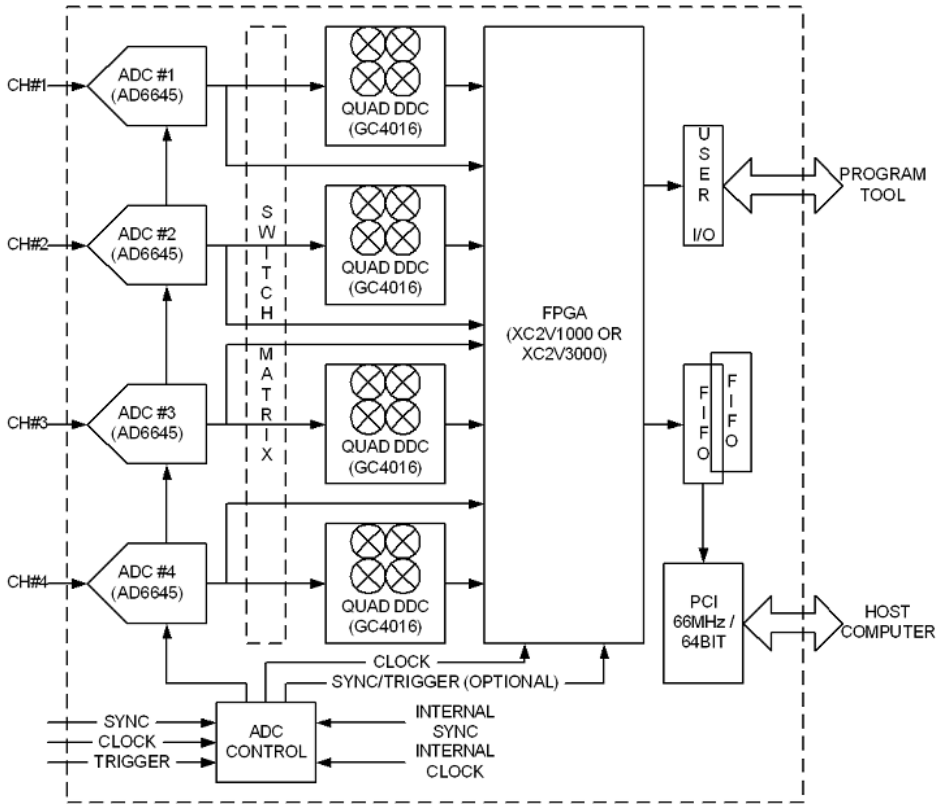


**Figure 6.6. Internal structure of the ICS554 digital receiver.** Structure of the digital receiver (ICS554) from Radstone-ICS. It contains up to four 14-bit ADCs (AD6645), and four quad-DDCs (GC4016). The FPGA can be programmed with custom signal processing logic. Details on the AD6645 and GC4016 are contained in Appendix E.

The ICS554 card is capable of producing downconverted data at a rate of 400 Mbyte/s. This rate easily surpasses the sustained write speed of a high-speed hard drive and, depending on the required processing, can overcome the processing capabilities of the computer. Consequently, the broadband receiver uses one dual-CPU computer for each ICS554 card. In addition, the nominal bandwidth of the ICS554 is limited to 1 MHz and its output data rate limited to 80 Mbyte/s.

The digital receiver incorporates four AD6645 14-bit ADCs, sixteen GC4016 DDCs, and a field-programmable-gate array (FPGA). Details of the AD6645 and GC4016 are found in Appendix E. A pulse on the trigger input initiates sampling by the ADCs at

a user-specified clock rate (between 30 MHz and 105 MHz). A pulse on the synchronization input ensures that all sixteen DDCs are processing data simultaneously[15] at the sampling rate.

Data from the ADCs can be fed straight to the output via the FPGA. If so, the output sampling rate is the sampling rate of the ADCs, but can be reduced by decimation at the ADC (see Appendix E for more detail). Usually though, data from the ADCs is fed to one or more of the DDCs through a switch matrix.

Each DDC performs signal downconversion and filtering. Up to 2 MHz within the 52.5 MHz bandwidth of the ADCs can be brought to baseband by the DDC. In-phase (I) and quadrature-phase (Q) components of the signal are output by mixing the incoming signal with a numerically controlled oscillator (NCO). The I and Q signals are then filtered and decimated. Three finite-impulse-response (FIR) filters can be applied to the downconverted signals prior to processing in the FPGA and/or forwarding on to the Data Processing module.

The FPGA performs the function of data formatting so that downconverted samples can reach the PCI bus of the host computer. The arrangement of data follows an I-Q-I-Q-...pattern, which represents an in-phase sample followed by a quadrature-phase sample. The first two samples are the I and Q samples from the first DDC, the second two samples are the I and Q samples from the second DDC, and so on for each DDC. Given that there are 16 DDCs, the period between successive I samples from a particular DDC is 32 samples.

The format of a sample is dictated by the configuration of the DDC such that any I or Q sample consists of a 32-bit word with three fields as in Figure 6.7. The data field contains a 20-bit value (see the GC4016 documentation in Appendix E on how this can be changed to 24-bits) representing the magnitude of the result produced by the DDC. The tag field contains a 4-bit code indicating from which DDC the sample came and whether the sample is an in-phase or quadrature-phase sample. The tags are also configurable. The padding field is ensures that the entire sample occupies an even number of bytes.

[15]The timing error between DDCs is approximately 50 ps.

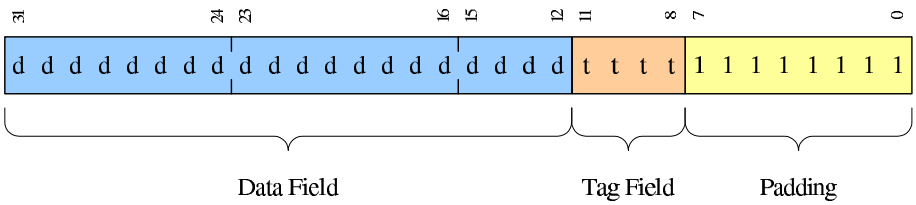


**Figure 6.7. Format of samples generated by the ICS554 digital receiver.** Format for each I and Q sample. The 32-bit sample has three fields: data, tag, and padding. The data field contains the value of the sample. The tag field can contain values from 0 to 15, which indicate whether the sample is an in-phase or quadrature sample and from which DDC the sample came. The tag field can be disabled if necessary. The padding field is used only to fill the entire sample so that it fits within an even number of bytes.

## Data Processing

The purpose of the data processing system is to analyze signals provided by the receiver system. It too is scaleable, and can be likened to a pool of computers and modular algorithms. Within this pool, computers and processing algorithms can be added to improve system performance. For example, computers are allocated tasks such as detection, enhancement, feature extraction, and tracking of signals as needed. Should one analysis routine prove unsuitable for a certain class of signals, another can be "switched in" that yields a better result. Some of the algorithms implementing these functions are proprietary. Discussion relating to the proprietary algorithms are therefore necessarily brief.

Detection is the process of determining whether or not an HF channel (nominally 3 kHz) contains detectable man-made signals. Channels that contain apparent signal energy are passed on to a signal enhancement routine, while those containing noise or signals of no interest are discarded. Part of the detection process uses the MUSIC (Gething 1991) and Capon (Gething 1991) direction-finding algorithms to determine the direction of signal energy impinging on the antenna array.

Signal enhancement attempts to improve the quality of signals passed to it by the detection process. Various methods are used to improve the signal-to-noise ratio of the signal, all of which are proprietary. Signals that are suitably enhanced are subsequently passed to feature extraction and tracking functions.

The tracking function follows the enhanced signal in frequency, time, and the hemispherical space above the antenna array. For example, the hemispherical location of

an HF signal emanating from an aircraft, moves with the aircraft. Ionospheric disturbances may also vary the direction and elevation of a signal.

Feature extraction is performed in parallel with signal tracking and is applied to an enhanced signal to aid automatic recognition of signal modulation. Among others, basic features include: the power-spectral density (PSD), an estimate of signal-noise ratio (SNR), and an estimate of bandwidth. And, by nature of the system architecture, various user-customizable features can be extracted. Some of these features might include statistical parameters such as variance, high-order moments and cumulants. Other custom features may be any of the host of parameters proposed in the literature (Aisbett 1986, Akmouche 1999, Carter 1993, Choi & Lee 2003, Hero III & Hadinejad-Mahram 1998, Hippenstiel & De Oliveira 1990, Hsue & Soliman 1990, Ketterer, Jondral & Costa 1999, Mitchell & Westerkamp 1999, Nandi & Azzouz 1997, Nandi & Azzouz 1998, Wong & Nandi 2001).

## Specific Equipment for Swan Reach

The equipment on which data is collected is a subset of the broadband receiver discussed in Section 6.3. Furthermore, the location of the test installation is some 150 km to the east of Adelaide near Swan Reach, South Australia. Figure 6.8 shows the location of Swan Reach relative to Adelaide, South Australia.

Eight passive monopoles (with elevated feed points) are arranged in a circular pattern, with seven equispaced antennas on the circle and the eighth at the centre. The radius of the circle is 20 m. The number and arrangement of antennas is irrelevant to this discussion, but are important for the Data Processing System.

The hut is a 3 m $\times$ 3 m $\times$ 6 m shipping container outfitted as a mobile laboratory. In this hut are two servers (one named OCTOPUS and the other named CUTTLEFISH)[16] each hosting one 4-input ICS554 digital receiver. Antenna feeders are connected to a wideband gain control system (see Section 6.3) that consists of wideband filters and variable gain stages. The system is capable of autonomous operation, but during the data collection (April 6–7,2006 and May 25–26, 2006) the gain was manually controlled.

[16]The naming of the two servers is perhaps related to the number of arms, in this case antennas, connected to the digital receivers, but in any case were chosen by Ebor Computing.

NOTE: This figure is included on page 72 of the print copy of the thesis held in the University of Adelaide Library.

**Figure 6.8. A satellite view of Swan Reach, South Australia.** A satellite view of South Australia, showing the location of Swan Reach and the broadband receiver and antenna array. Swan Reach is approximately 150 km north-east of Adelaide at 34° 34' 0" S latitude and 139° 34' 60" E longitude. The receiver site is about 20 km east of Swan Reach (figure adapted from Google™ Maps).

The digital receiver in one server (OCTOPUS) is setup in *master* mode. This means that the ICS554 generates timing signals for the ICS554 hosted by the other server (CUTTLEFISH). Consequently, the ICS554 in CUTTLEFISH is configured for operation in slave mode. In this mode the ICS554 expects to receive its timing information from an external source.

This timing information consists of a sampling clock, a sampling trigger, and a synchronization pulse. The sampling clock, called CLOCK, is a 100 MHz sinusoid. The ADCs in the ICS554 sample once per period of this clock. The sampling trigger (of which there is only one) initiates sampling by the ADCs. The synchronization pulse (of which there is only one) ensures that DDCs on both cards are processing simultaneously. The coaxial cables carrying the synchronization pulse and trigger pulse are as short as possible to minimize the time delay. These cables are RG58 type and have a characteristic impedance of 50 Ω, a velocity propagation constant of 0.66, and length of 0.35 m. Each cable therefore introduces a delay of 1.76 ns to the pulse being conveyed by the cable. Originally, the coaxial cable for the sampling clock was also a 0.35 m length of RG58 cable. However at 100 MHz, a 1.76 ns delay corresponds to a 19° phase

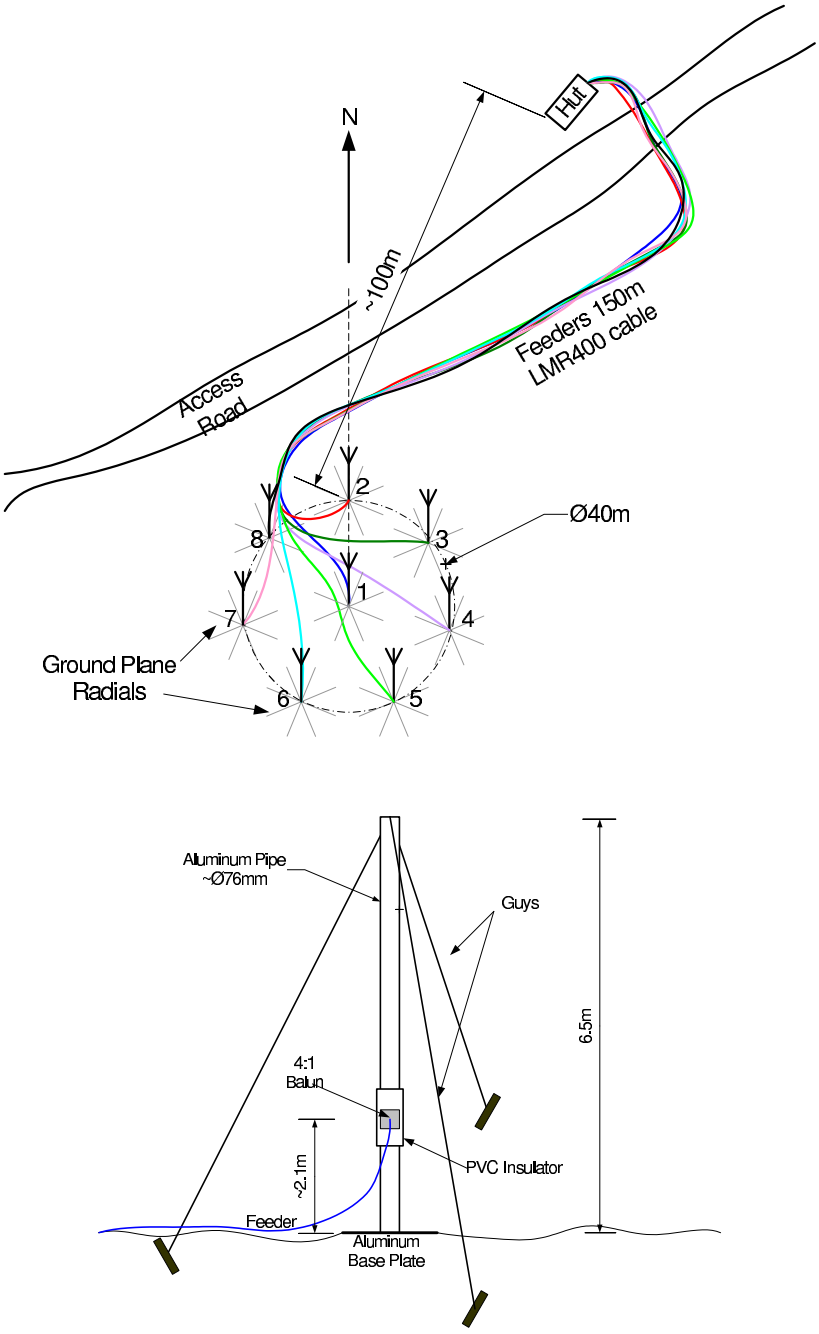


**Figure 6.9. Array configuration and antenna construction at Swan Reach.** Configuration of array at test site (*top*); antenna construction (*bottom*). The circular arrangement of antennas balances the inter-element coupling effects of all the antennas, and is important for the Data Processing System. The antenna construction is an elevated feed vertical monopole. The antenna design caters for signals towards the upper part of the HF band, but its low-HF band performance is sufficient for the sake of this work, For data collected in April 2006, the feed from antenna 3 was weak. It was not used in the PDF calculations.

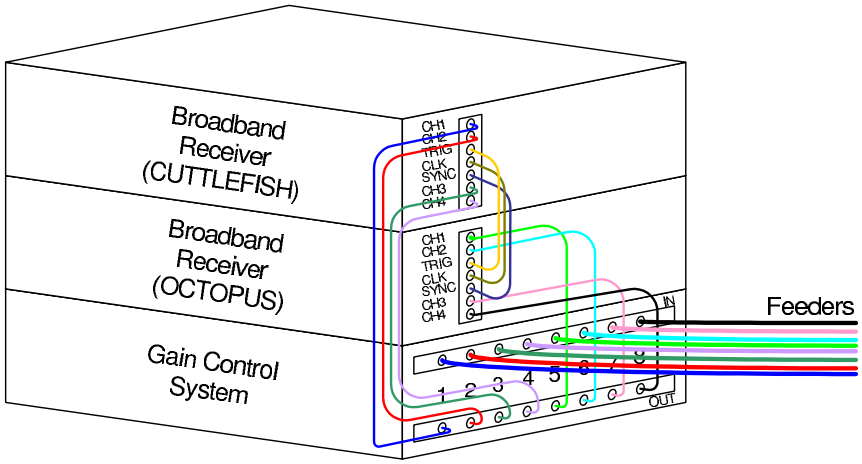


**Figure 6.10. Connections for broadband receivers at Swan Reach.** Connections for the broadband receivers inside the hut at Swan Reach are shown here. Feeders from the antennas are connected to the inputs of the gain control system, the outputs of which are fed to two 4-input ICS554 digital receiver cards. Each ICS554 is housed in a dual-CPU server. These servers store the baseband information provided by the ICS554 cards. The ICS554 in OCTOPUS provides timing information for the ICS554 in CUTTLEFISH. HF signals are sampled at 100 MHz.

shift between HF signals sampled by the *master* and *slave* receivers. This phase shift was unacceptable for the Data Processing System, though of no great importance for the current discussion. The length of cable was therefore increased to a full wavelength of the sampling clock to ensure that *master* and *slave* receivers were sampling on the same clock edge. The correct cable length is 1.98 m. The delay affecting the trigger and synchronization pulses have no real effect because they are synchronized with the rising edge of the sampling clock and sampling occurs on the falling edge of the sampling clock.

Software running on OCTOPUS and CUTTLEFISH configure the ICS554 cards to acquire samples at 100 MHz, and then downconvert a 153.6 kHz complex bandwidth, centred at the frequency of interest, to baseband. This process is performed simultaneously for signals acquired by all the antennas. For this data collection only four DDCs are used per ICS card; the ICS554 is able to provide downconverted complex bandwidths up to 2 MHz for each of its 16 DDCs. That is, the ICS554 can provide 16 independent and downconverted 2 MHz complex bandwidths between 1.6 MHz and 50 MHz. The lower limit is imposed by the design of the ICS554 hardware and the upper limit is dictated by the sampling theorem. Together, two ICS554 cards can generate

data a rate of 1,024 MB/s. In the current configuration, each ICS554 card generates 4.9 MB/s of data (153.6 kHz $\times$ 4 DDCs/card $\times$ 4-bytes/sample $\times$ 2 channels/DDC).

The ICS554 is a PCI Mezzanine Card (PMC). In the hardware configuration for the broadband receiver, the ICS554 mounts onto a Technobox 3763 PMC-PCI carrier card. This carrier card mates the PMC form-factor to the 64-bit PCI bus (at 66 MHz) in the host computer. And, though the 64-bit PCI bus (at 66 MHz) is capable of handling 528 MB/s, most hard-disks cannot store data at this rate. As a result of this fact, and for additional reasons important only to the Data Processing System, the 153.6 kHz complex bandwidth was chosen as the most suitable bandwidth to acquire for each DDC.

Though the ICS554 interleaves samples from all DDCS in the form of I0, Q0, I1, Q1, I2, Q2,..., the software running on OCTOPUS and CUTTLEFISH de-interleaves the samples so that they end up in individual files. Each file contains all of the I and Q samples from a particular DDC. When data is read from each file the lower 12-bits of each sample are stripped away to get the magnitude of each sample.

The entire RF chain is shown in Figure 6.11. The passive antenna has a mismatch loss depicted in see Figure 6.12. The gain of the antenna is approximately 0 dBi and mismatch loss is the reduction in antenna gain due to impedance mismatch between antenna and feeder cable. Therefore the mismatch loss represents the gain of the antenna, $G_a$.

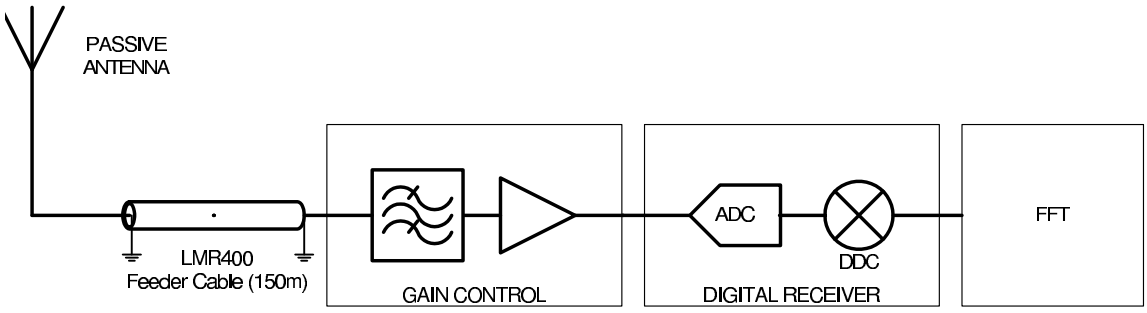


**Figure 6.11. Model of RF chain used for data collection at Swan Reach.** The RF chain for data collection at Swan Reach is similar to that used in the swept-narrowband method. The main difference is the antenna construction, and processing. Data output from the DDC is converted to the spectral domain for processing.

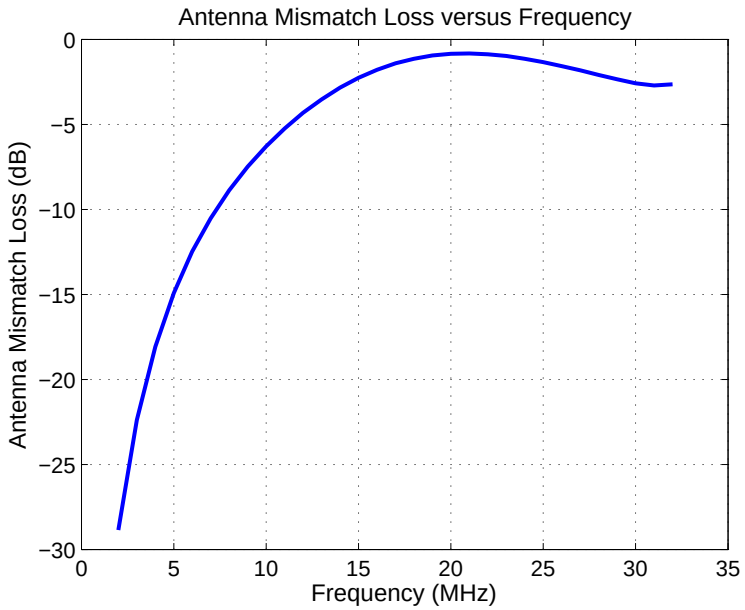


**Figure 6.12. Mismatch loss for antennas at Swan Reach.** Mismatch loss versus frequency for passive antenna. The passive antenna is a replica of a 6.5 m antenna produced by Radio-Frequency Systems (RFS) in Melbourne, Australia. The diagram above is the mismatch loss of the RFS antenna. It is assumed that the replica antenna has the same mismatch loss. Mismatch loss is the reduction in antenna gain due to impedance mismatches. The gain of the replica antenna is approximately 0 dBi and therefore the mismatch loss represents the gain of the replica antenna.

The feeder gain (repeated here for convenience) is the negative of feeder loss and is dictated by the cable manufacturer (Times Microwave) as

$$G_{\mathrm{f}} = \frac{1250L}{381}\left(0.12229\sqrt{F} + 0.00026F\right), \tag{6.4}$$

where $F$ is frequency in MHz, $L$ is cable length in meters, and $G_{\mathrm{f}}$ has units of dB. The gain of the feeder varies from approximately $-1$ dB at 3 MHz to approximately $-3.5$ dB at 32 MHz. The feeder gain is shown in Figure 6.3.

The gain, $G_{\mathrm{gc}}$ of the gain control system is controlled manually. The gain setting for each data collection session is listed in Tables B.1 and B.2. Although, the indicated gains are those of the amplifier only, the losses introduced by the filtering in the pass-band are negligible. Note also that the noise figure of the gain control systems changes with the gain settings (see Appendix C).

Gain of the ICS554 consists of four components: ADC transducing gain, DDC numerical gain, DDC processing gain, and FFT processing gain. The ADC transducing gain provides the conversion from an analog voltage to a digital value. In a real sense there is no power gain through the ADC, but since samples at the output for the ICS554 are referenced back to an electric field strength at the antenna, an artificial power gain is necessary. To determine the power gain the ratio of the output power to the input power is required. The input power is simply

$$P_{\text{in}} = \frac{v_{\text{in}}^2}{Z}, \tag{6.5}$$

were $v_{\text{in}}$ is the input voltage across the ADC input impedance, $Z$. By ignoring the nonlinear aspects of the ADC, the output of the ADC is related to its input voltage by,

$$v_{\text{out}} = \frac{2^M}{V_{\text{FS}}} \times v_{\text{in}}, \tag{6.6}$$

where $M$ is the number of bits of the ADC, $v_{\text{in}}$ is the input voltage, and $V_{\text{FS}}$ is the full-scale input voltage for the ADC. The output of the ADC is treated as a voltage referenced to an arbitrary impedance of 1 Ω, even though impedance has no meaning in the digital domain, therefore the output power is

$$P_{\text{out}} = \left( \frac{2^M}{V_{\text{FS}}} \times v_{\text{in}} \right)^2. \tag{6.7}$$

Taking the logarithm of the ratio of Eq. (6.7) to Eq. (6.5) yields the artificial power gain

$$G_{\text{ADC}} = 10 \log_{10} Z + 20M \log_{10} 2 - 20 \log_{10} (V_{\text{FS}}). \tag{6.8}$$

For the AD6645 $Z = 50\ \Omega$, $M = 14$, and $V_{\text{FS}}$ is 1.2 V, so $G_{\text{ADC}}$ is 99.7 dB.

**Table 6.1. Configuration parameters for the GC4016.** The primary configuration parameters for the GC4016 DDC in the test setup, which is a subset of the broadband receiver. The value for each parameter follows a set of rules dictated by the GC4016 data sheet (page reference in the **Page** column).

| Mneumonic | Value | Description | Page |
|---|---|---|---|
| N or DEC | 163 | CIC filter decimation ratio | 39 |
| CFIR_SUM | 56695 | Sum of coefficients of Complementary FIR filter (100% filter) | 57 |
| PFIR_SUM | 60221 | Sum of coefficients of Peripheral FIR filter (100%filter) | 58 |
| NZEROS | 0 | Number of zeros inserted in blank mode | 38 |
| SHIFT | 7 | Value to shift mixer output (range 4 to 7) | 37 |
| SCALE | 0 | Small scaling factor (range 0 to 5) | 39 |
| BIG_SCALE | 3 | Big scaling factor (range 0 to 7) | 39 |
| FINE_GAIN | 1024 | Gain prior to PFIR | 41 |
| RES_SUM | 32768 | Sum of coefficients of Resampler FIR (bypass mode) | 60 |
| NDELAY | 1 | Resampler interpolation factor (bypass mode) | 60 |
| FINAL_SHIFT | 5 | Number of bits to shift the output sample (range 0 to 15) | 44,60 |
| COARSE | 1 | Number of bits of gain prior to CFIR | 40 |

The data sheet (see Appendix E) for the GC4016 DDC shows the equivalent voltage gain through the DDC as

$$\begin{aligned} G_{\mathrm{DDC}} = {} & 10\log_{10}\left[\left(\frac{\mathrm{N}^5}{\mathrm{NZEROS}+1}\times 2^{(\mathrm{SHIFT}+\mathrm{SCALE}+6\times\mathrm{BIG\_SCALE}-62)}\right)\right] \\ & + 10\log_{10}\left[(2^{\mathrm{COARSE}})\left(\frac{\mathrm{CFIR\_SUM}}{65536}\right)\left(\frac{\mathrm{PFIR\_SUM}}{65536}\right)\right] \\ & + 10\log_{10}\left[\left(\frac{\mathrm{FINE\_GAIN}}{1024}\right)\left(\frac{\mathrm{RES\_SUM}}{32768\times\mathrm{NDELAY}}\right)(2^{\mathrm{FINAL\_SHIFT}})\right]. \end{aligned} \tag{6.9}$$

With the parameters specified in Table 6.1, the DDC voltage gain is 16.5 dB. The equivalent power gain, $G_{\mathrm{DDC}}$, is twice this value at 33 dB (again referenced to 1 Ω).

The total system power gain is then

$$G_{\mathrm{T}} = G_{\mathrm{a}} + G_{\mathrm{f}} + G_{\mathrm{gc}} + G_{\mathrm{ADC}} + G_{\mathrm{DDC}}, \tag{6.10}$$

and it is now possible to refer the output samples of the DDCs back to the antenna and thereby convert them to a $\mu$V/m measure.

## 6.4 Summary

This chapter describes the test setup for measuring the PDF of HF noise. Two different setups are used: one a narrowband receiver and the other a multi-antenna broadband receiver. The two receivers have some common components but do not process HF signals in the same way. The narrowband receiver (bandwidth of approximately 4 kHz) is swept in time and frequency whereas the broadband receiver, used for data collection, stares at a specific 153.6 kHz bandwidth in the HF band.

The narrowband receiver was developed and used to collect data by Brine *et al* (2002) as part of a pre-emptive null-steering ionosonde. The broadband receiver was developed and manufactured by Ebor Computing.

Having described the receiving equipment, the topic now turns to the results of applying methods in the previous chapter to the data collected via the receivers. Chapter 7 is devoted to this issue.

Chapter 7

# HF Noise

IN this chapter procedures for determining the probability density function (PDF) of HF noise (see Chapter 5) are applied to data sets collected in Adelaide and near Swan Reach, South Australia. The swept-narrowband method is applied to the Adelaide data set while the broadband method is applied to the Swan Reach data set.

Both data sets show that the PDF of HF noise is generally not Gaussian. It appears to follow a Bi-Kappa distribution, which is peaked and impulsive. Moreover, the PDF has diurnal variations and is affected by man-made groundwave and skywave interference. Significant man-made interference tends to add a Gaussian component to the PDF. This Gaussian component is strong in urban areas and weaker in remote country locations.

## 7.1 Introduction to Results

Previous chapters outline methods and describe equipment by which the PDF of natural HF noise[17] can be measured. There appears relatively little description in the literature of methods for measuring the PDF, certainly nothing similar to that described in this thesis. The results presented here and the methods to acquire them are therefore unique. But more importantly, the results show that the statistics of HF noise are different from the common assumption of additive white-Gaussian noise for modelling of the HF channel.

Two sections follow that describe the PDF of natural HF noise. Section 7.2 considers the PDF in an urban area. The analysis shows two visible components in the noise PDF. Section 7.3 illustrates more clearly the natural HF noise in a remote environment.

## 7.2 Results of the Swept-Narrowband Method

Consider Figure 7.1 which shows the PDF of HF noise between 6.1 MHz and 6.3 MHz for various times shortly after sunrise. The sub-channel bandwidth, $BW_c$, is 1.2 kHz and the bandwidth over which the noise statistics are assumed stationary in the wide sense, BW, is 228 kHz (these choices of bandwidth are reasonable for the purpose of this demonstration). From 7:00 am to 8:00 am the PDFs are decidedly non-Gaussian because most noise emitting sources have not yet been turned on (people are just waking). During this time the D-region is becoming more ionized and is absorbing sky-wave transmissions. After 8:00 am the PDF becomes more and more Gaussian. This is indicative of nearby emitters of all types[18] contributing to the noise background as people begin enabling their electrical devices. It is well known, via the central-limit theorem, that the sum of many independent and identically distributed random variables tends to a Gaussian distribution. Consequently, environmental noise through ground-wave transmissions are likely affecting the PDF after sunrise due to the fact that the D-region is absorbing most distant environmental and natural sources of noise. In addition, the local environmental noise is also increasing in amplitude.

[17] Recall that the definition of natural HF noise includes all HF noise except that caused by man.
[18] These transmitters could be genuine HF transceivers, or welders and car ignitions for example.

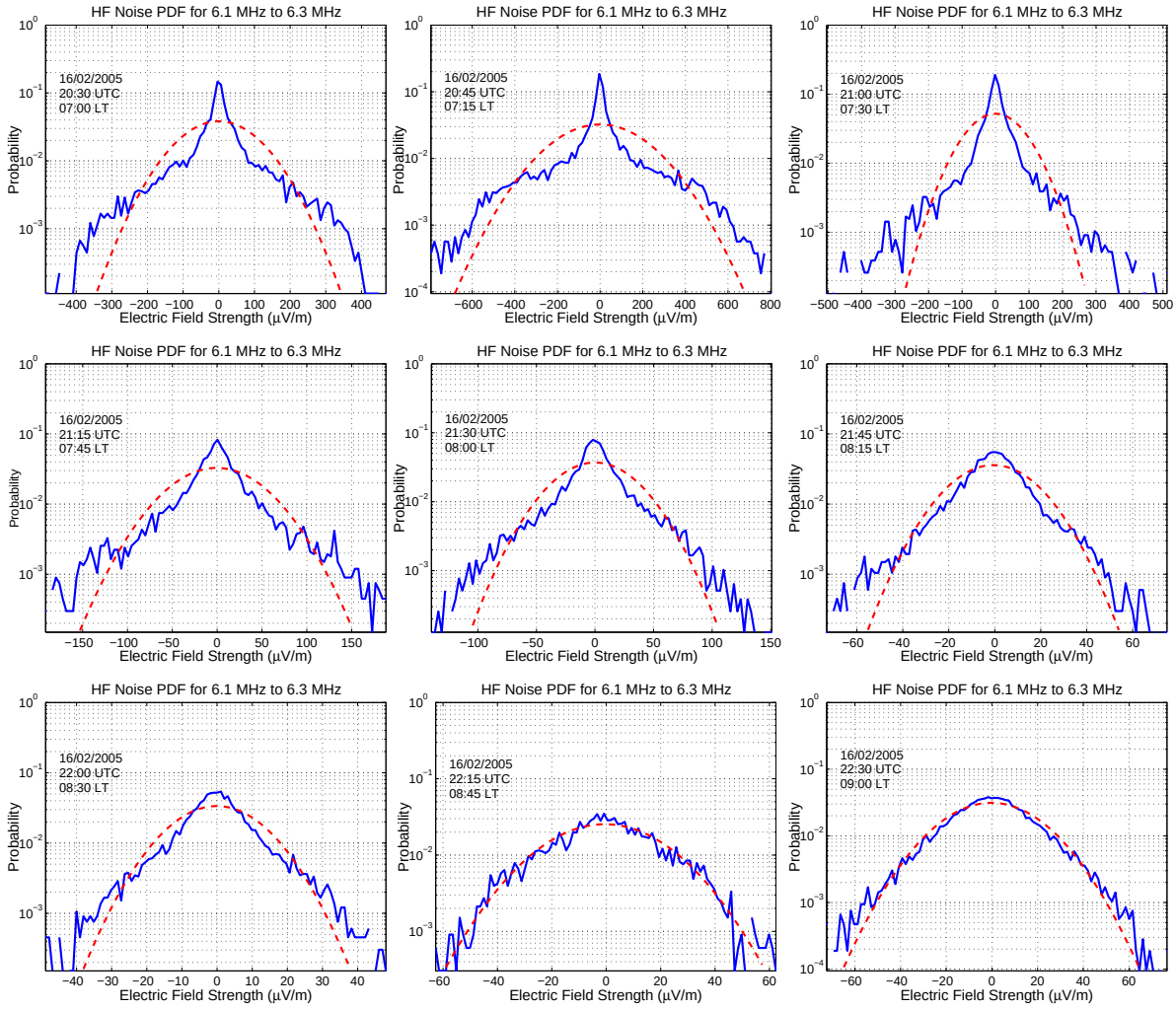


**Figure 7.1. PDF of HF noise measured by the swept-narrowband method.** Probability versus electric field strength (vertical component) of HF noise in a 4 kHz band across the electronic length of the antenna for various times shortly after sunrise. The local time (LT) is 06:51 hr and observation frequencies vary from 6.1 MHz to 6.3 MHz. A Gaussian PDF is superimposed (dashed curves) to show how poorly it fits the PDF of HF noise prior to 08:45 hr local time. Notice that as the day progresses the PDF becomes more and more Gaussian. This is indicative of transmitters of all types contributing to the noise background as people awake and begin enabling their devices. It is well known, via the central-limit theorem, that the sum of many independent and identically distributed random variables tends to a Gaussian distribution. The units of noise ($\mu$V/m) can be converted to $V^2$/Hz with knowledge of the electronic length of the antenna at each frequency.

Similar results are achieved for the PDF at frequencies between 11.6 MHz and 11.8 MHz, as well as between 13.6 MHz and 13.8 MHz. At the urban measurement site, the PDF

at frequencies between 5.4 MHz and 5.6 MHz is markedly Gaussian at all times. This band has high signal levels throughout the day.

All of this suggests that the assumption of Gaussian noise can lead to inaccurate measures of algorithm or model performance. Consequently any HF communications model must account for the surrounding HF environment (*i.e.* mixture and strength of noise and interference components), the frequency band, and the time of day. However, given the enormous difficulties involved in developing robust modulation recognition algorithms, it is not unreasonable to begin with an assumption of Gaussian noise and then to progress to a more realistic form of noise.

## 7.3 Results of the Broadband Method

The results presented here, based on data collected near Swan Reach (see Appendix B), lend further evidence to the results in the previous section. In fact, Swan Reach proved to be an excellent location for acquiring data on HF signals and HF noise. Almost every probability density function below testifies of the quiet site—quiet in the sense that the level of environmental noise is low. Intuitively, a quiet HF site suggests that the PDF of HF noise has a narrow peak because there is little environmental noise. Man-made noise can be a dominant component of HF noise, especially near places of human habitation. But, at a quiet site the environmental component nearly disappears and the residue is mainly the atmospheric and galactic noise. Indeed, that is what appears to happen in the results soon to be discussed.

One issue not raised previously, is the effect of band allocation on the noise PDF. That is, in countries participating in the ITU allocation of HF spectrum, particular HF transmissions are confined to specific bands. For example, the 15 m band for amateur radio operators is 21 MHz to 21.45 MHz (see Appendix F). Of the many band allocations, the bands reserved for amateur, aeronautical, broadcasting, and maritime communications are some of the most congested. Parts of the data from Swan Reach are in congested bands. The broadband method removes most man-made signals, but in the congested bands many weak man-made signals may not be removed by the method. In some cases the 153.6 kHz bandwidth of the broadband receiver straddles more than

one band allocation. Therefore, it is expected that some of the results below may exhibit a small Gaussian component in the shoulders of the PDF. One would also expect this behaviour when considering the implications of the central limit theorem.

## Results from 6–7 April 2006

Figure 7.2 shows the PDF of HF noise from about 1700 hr to 1830 hr local time on April 6, 2006. The PDF in part a) of the figure should be rejected for two reasons. The PDF is based on approximately 1 min of data[19], which is not enough to create a statistically significant PDF in comparison with the longer data sets of the other PDFs in the figure. Note the narrow range of the electric field strength and compare it to the other sub-figures. This is typical of a result based on too few samples. Secondly, the data set covers a broadcast band (15.1 MHz to 15.6 MHz) and a standard time/frequency band (14.99 MHz to 15.01 MHz). Broadcast bands are generally congested with transmissions. So, even though the broadband method may remove most of the congestion, weak man-made signals may still contaminate the PDF. This contamination is the likely reason for the Gaussian-like shoulders of the PDF. Nevertheless, the other sub-figures exhibit a shape similar to the Bi-Kappa distribution.

Note, sub-figures b), c), and d). The PDF in each of these plots has the markedly peaked shape expected of HF noise, indeed very much like the Bi-Kappa shape described in the previous section. The standard deviation of the electric field strength is shown in each sub-figure. The HF noise power density can be calculated from the standard deviation (or root-mean-square) of the electric field strength and an assumed characteristic impedance of the transmission medium at the input to the antenna. This calculation of noise power density in a 1 kHz bandwidth is

$$P_{\mathrm{n}} = 10\log_{10}\left[\frac{\left(\sigma \times \frac{1\ \mathrm{V}}{10^6\ \mu\mathrm{V}}\right)^2}{Z_o} \times \frac{1000\ \mathrm{mW/W}}{1\ \mathrm{mW/m^2}}\right] - 10\log_{10}\left(\frac{153.6\ \mathrm{kHz}}{1\ \mathrm{kHz}}\right), \qquad (7.1)$$

where $\sigma$ is the RMS electric field strength ($\mu$V/m) in a 153.6 kHz bandwidth[20], $Z_o$ is the characteristic impedance of the air transmission medium (assumed to be that of

[19] Table B.1 indicates that the data set is for operational test purposes; hence the short time span.
[20] Recall that the bandwidth of the broadband receiver is 153.6 kHz.

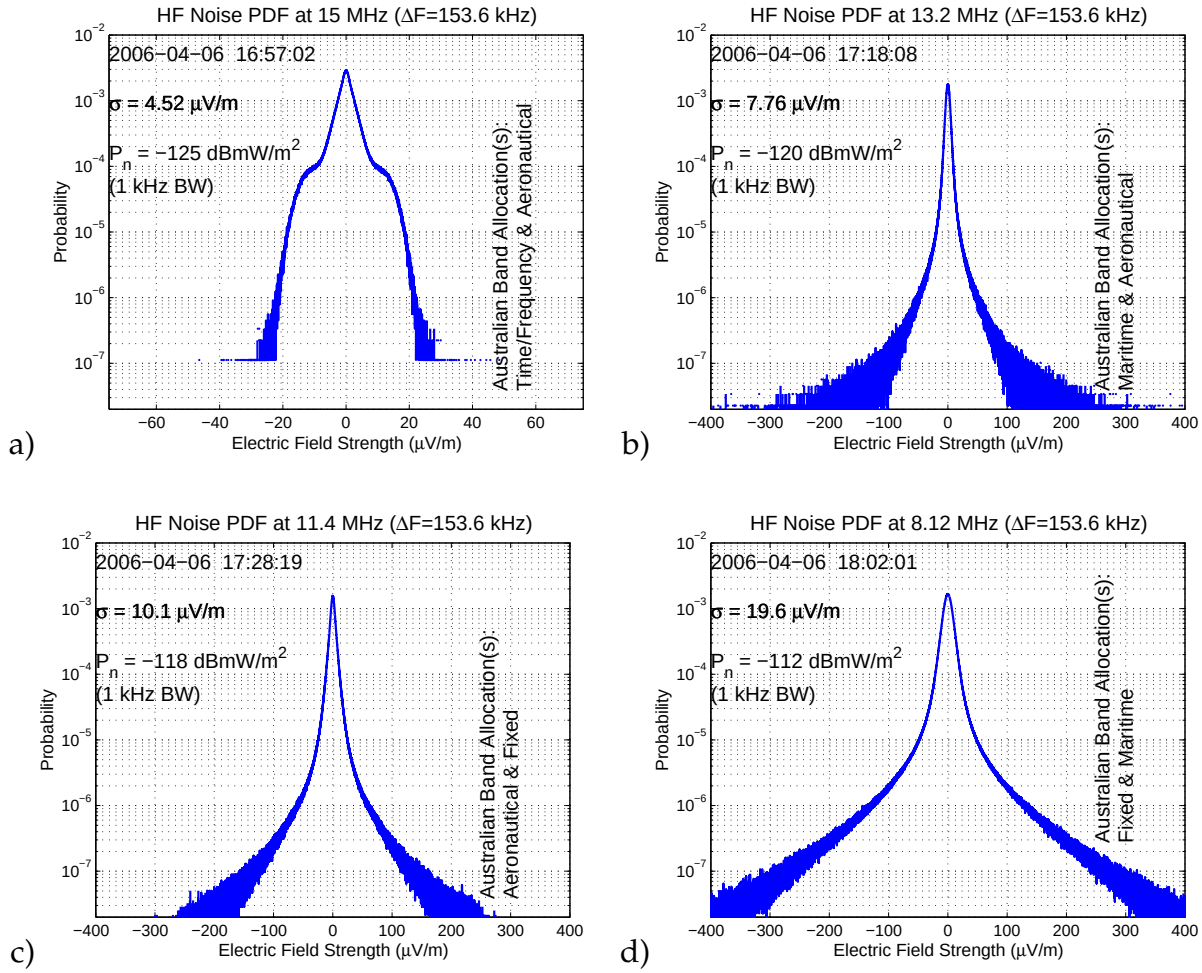


**Figure 7.2. The PDF of HF noise—06 April 2006, 17:00 hr to 18:30 hr local time.** Probability density functions for HF noise near Swan Reach, South Australia on 06 April 2006 from 17:00 hr to 18:30 hr local time. The timestamp for each PDF indicates the time at which a 30 min (nominal) data recording began. However, in this figure, part a) is based on only 1 min of data, and part b) 12 min of data (see Appendix B for more information). The bandwidth of the data source is 153,600 Hz (a function of the design of the broadband receiver at Swan Reach) and the centre of the band is indicated in the title of the sub-figure. The band allocation (see Appendix F) indicates that the data for the PDF may contain signals corresponding to the listed band type(s). The variable $\sigma$ represents the RMS electric field strength in the 153.6 kHz bandwidth, and $P_n$ is the noise power density (in a 1 kHz bandwidth) computed by Eq. (7.1).

free space, 376 Ω) at the antenna input, and $P_n$ is the noise power density in units of dB with respect to 1 mW/m$^2$ (denoted by dBmW/m$^2$). The last term in the equation represents a reduction in the noise power density due to the processing gain achieved by narrowing the bandwidth from 153.6 kHz to 1 kHz.

It is worth noting that each PDF is plotted against the electric field strength (vertical component) of the noise. In electronics, noise is often quoted in units of V$^2$/Hz (a measure of noise density). Knowing the bandwidth of the receiver and the electronic length of the antenna at each frequency, the probability densities can be plotted against noise density rather than field strength. The former method is more common in RF electronics and is therefore assumed in this thesis.

The probability density function of HF noise at other times on 06 April 2006 are shown in Figure 7.3 (18:30 hr to 20:30 hr) and Figure 7.4 (20:30 hr to 23:00 hr). These also exhibit the peaked shape expected of HF noise.

Figure 7.5 contains the PDFs measured on the next day, 07 April 2006, from 04:30 hr to 06:30 hr. Sub-figure a) exhibits rounded shoulders suggesting a Gaussian component to the PDF. It is well known that noise field strengths at low frequencies is greater than at higher frequencies. In fact, the 4.6 MHz band is well used for aeronautical communications. Before sunrise, the D-region is not formed and distant multi-hop signals could be sensed by the antennas. These distant signals could well be small enough to pass beneath the 3% threshold of the broadband method, thereby contaminating the noise PDF.

Sub-figure a), of Figure 7.6, is another example of a PDF based on too few samples. Note the narrow range of electric field strength indicating the small sample set. Table B.1 shows that the set contains approximately 2 min of data and that the broadband receiver was tuned to the wrong centre frequency.

Now consider the probability density functions in sub-figures b) and c). These appear to have a slight Gaussian shape in the tails of the PDFs. It is plausible that the weak signals from the aeronautical band, covered by the former, and the maritime band, covered by the latter, are contaminating the probability density functions.

Sub-figures b) and c) of Figure 7.7 also display an apparent Gaussian component. Again, the sub-figures cover aeronautical and maritime bands, though, the Gaussian component is much lower than in Figure 7.6 (*c.f.* probability of $10^{-7}$ *versus* the probability of $10^{-6}$ to $10^{-5}$). The D-region is formed during the morning daylight hours and, during the time for the data set of Figure 7.6, is most likely attenuating distant aeronautical and maritime signals. These signals, weak as they are, pass through the broadband method to contaminate the PDF and form Gaussian shoulders.

Figures 7.2 to 7.8 show that, with few exceptions, the HF noise PDF is not Gaussian at sites with low-levels of environmental noise. At such sites the PDF is peaked and shows a strong dominance of low-level noise, with occasional bursts of high-level noise.

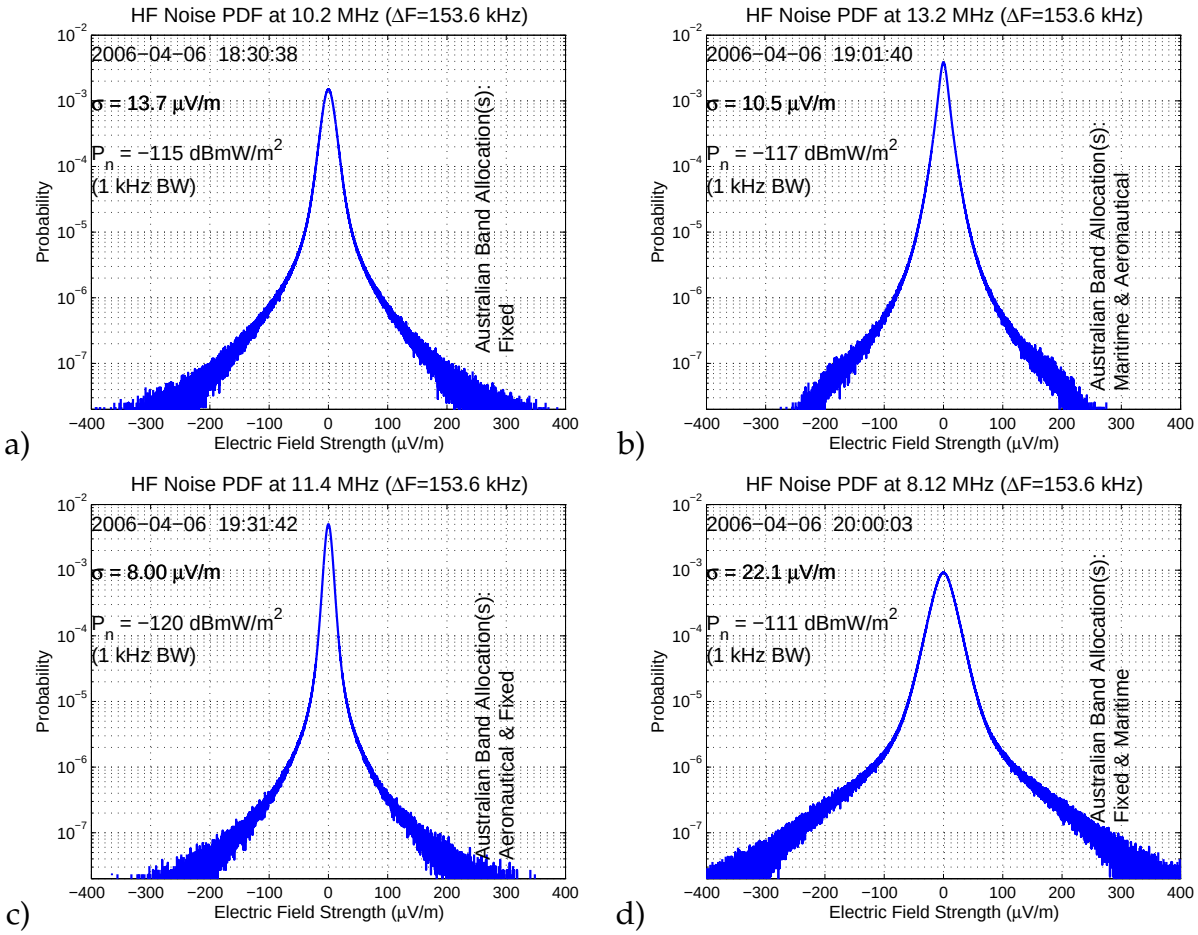


**Figure 7.3. The PDF of HF noise—06 April 2006, 18:30 hr to 20:30 hr local time.** Probability density functions for HF noise near Swan Reach, South Australia on 06 April 2006 from 18:30 hr to 20:30 hr local time. The timestamp for each PDF indicates the time at which a 30 min (nominal) data recording began. The bandwidth of the data source is 153,600 Hz (a function of the design of the broadband receiver at Swan Reach) and the centre of the band is indicated in the title of the sub-figure. The band allocation (see Appendix F) indicates that the data for the PDF may contain signals corresponding to the listed band type(s). The variable $\sigma$ represents the RMS electric field strength in the 153.6 kHz bandwidth, and $P_n$ is the noise power density (in a 1 kHz bandwidth) computed by Eq. (7.1).

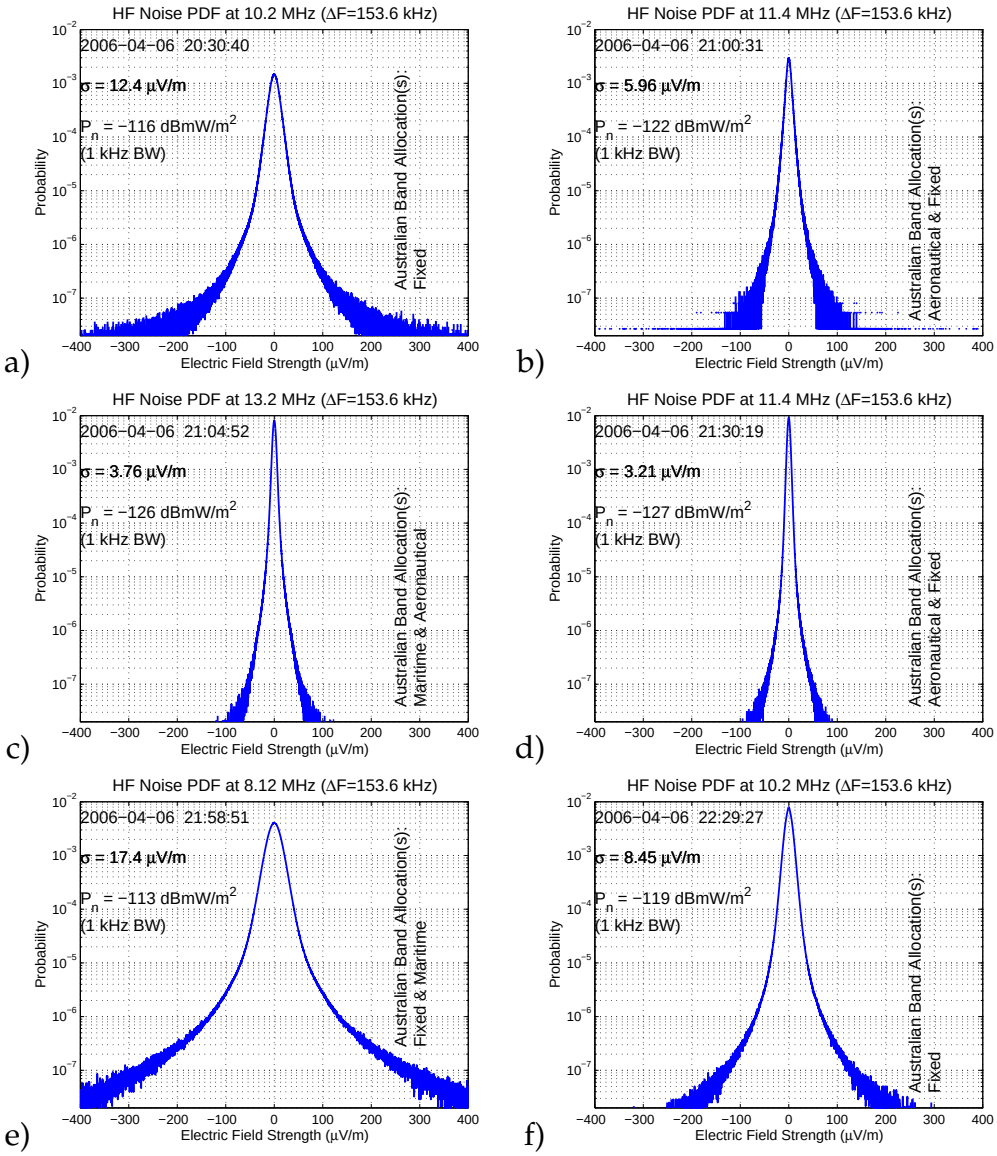


**Figure 7.4. The PDF of HF noise—06 April 2006, 20:30 hr to 23:00 hr local time.** Probability density functions for HF noise near Swan Reach, South Australia on 06 April 2006 from 20:30 hr to 23:00 hr local time. The timestamp for each PDF indicates the time at which a 30 min (nominal) data recording began. The bandwidth of the data source is 153,600 Hz (a function of the design of the broadband receiver at Swan Reach) and the centre of the band is indicated in the title of the sub-figure. The band allocation (see Appendix F) indicates that the data for the PDF may contain signals corresponding to the listed band type(s). The variable $\sigma$ represents the RMS electric field strength in the 153.6 kHz bandwidth, and $P_\mathrm{n}$ is the noise power density (in a 1 kHz bandwidth) computed by Eq. (7.1).

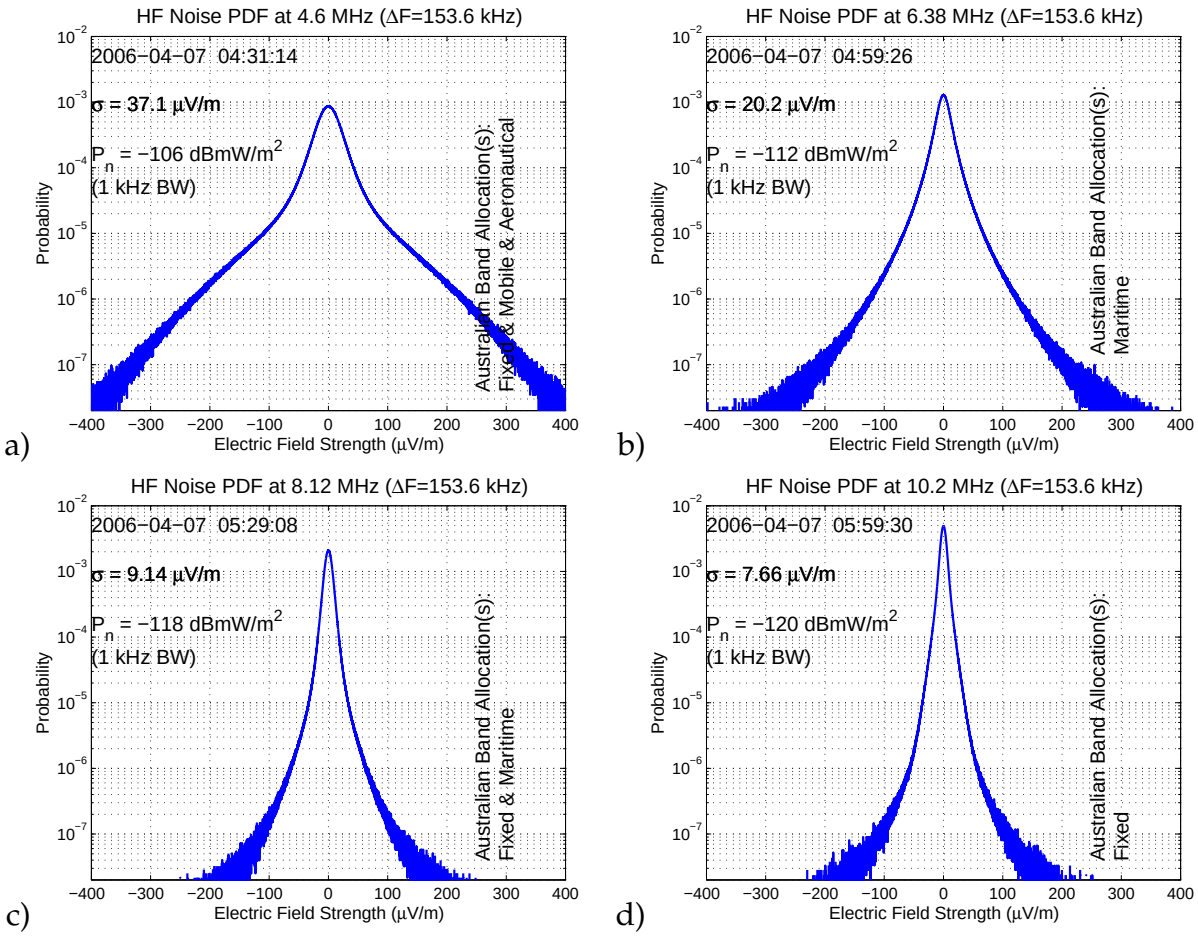


**Figure 7.5. The PDF of HF noise—07 April 2006, 04:30 hr to 06:30 hr local time.** Probability density functions for HF noise near Swan Reach, South Australia on 07 April 2006 from 04:30 hr to 06:30 hr local time. The timestamp for each PDF indicates the time at which a 30 min (nominal) data recording began. The bandwidth of the data source is 153,600 Hz (a function of the design of the broadband receiver at Swan Reach) and the centre of the band is indicated in the title of the sub-figure. The band allocation (see Appendix F) indicates that the data for the PDF may contain signals corresponding to the listed band type(s). The variable $\sigma$ represents the RMS electric field strength in the 153.6 kHz bandwidth, and $P_{\mathrm{n}}$ is the noise power density (in a 1 kHz bandwidth) computed by Eq. (7.1).

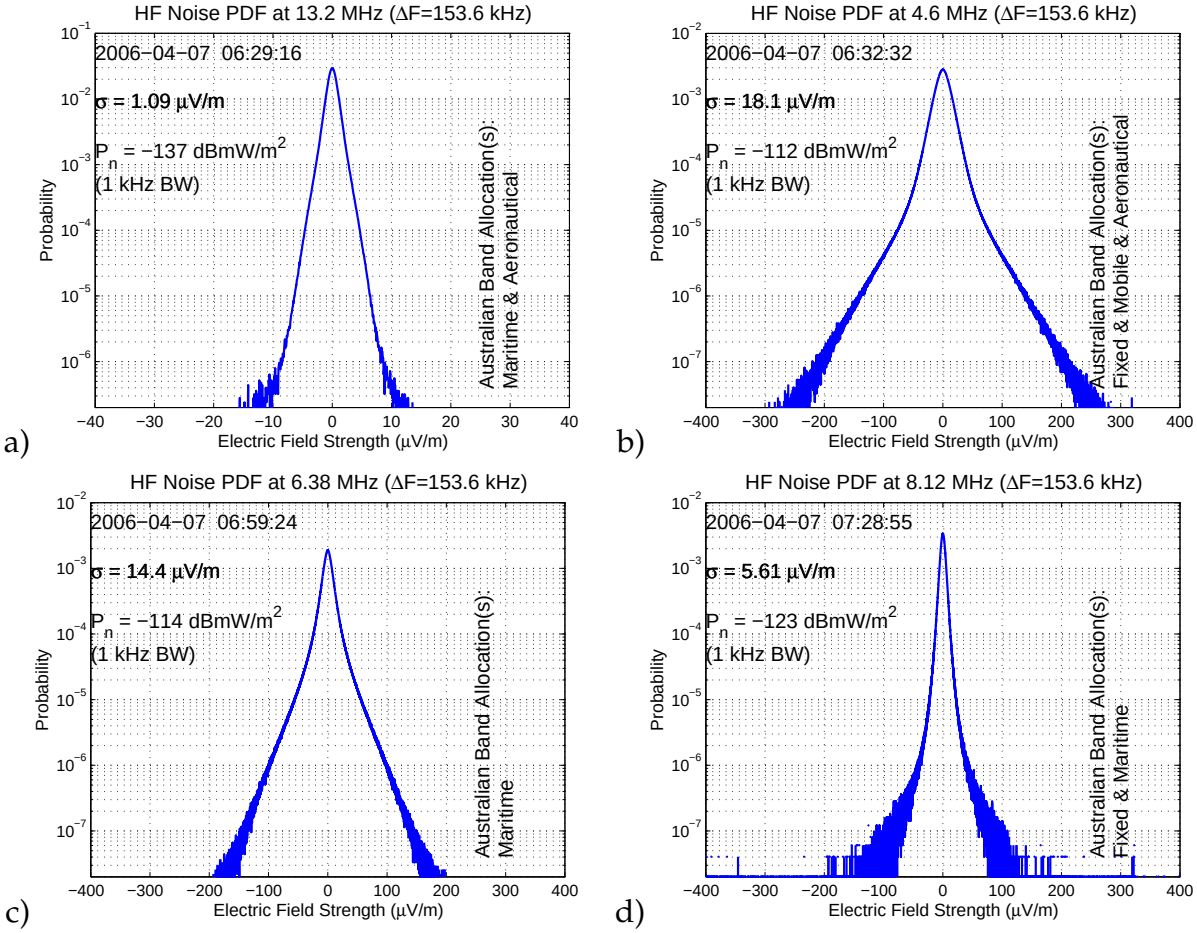


**Figure 7.6. The PDF of HF noise—07 April 2006, 06:30 hr to 07:30 hr local time.** Probability density functions for HF noise near Swan Reach, South Australia on 07 April 2006 from 06:30 hr to 07:30 hr local time. The timestamp for each PDF indicates the time at which a 30 min (nominal) data recording began. However, in this figure, part a) is based on approximately 2 min of data. Sub-figure d) is based on approximately 5 min of data. The bandwidth of the data source is 153,600 Hz (a function of the design of the broadband receiver at Swan Reach) and the centre of the band is indicated in the title of the sub-figure. The band allocation (see Appendix F) indicates that the data for the PDF may contain signals corresponding to the listed band type(s). The variable $\sigma$ represents the RMS electric field strength in the 153.6 kHz bandwidth, and $P_{\mathrm{n}}$ is the noise power density (in a 1 kHz bandwidth) computed by Eq. (7.1).

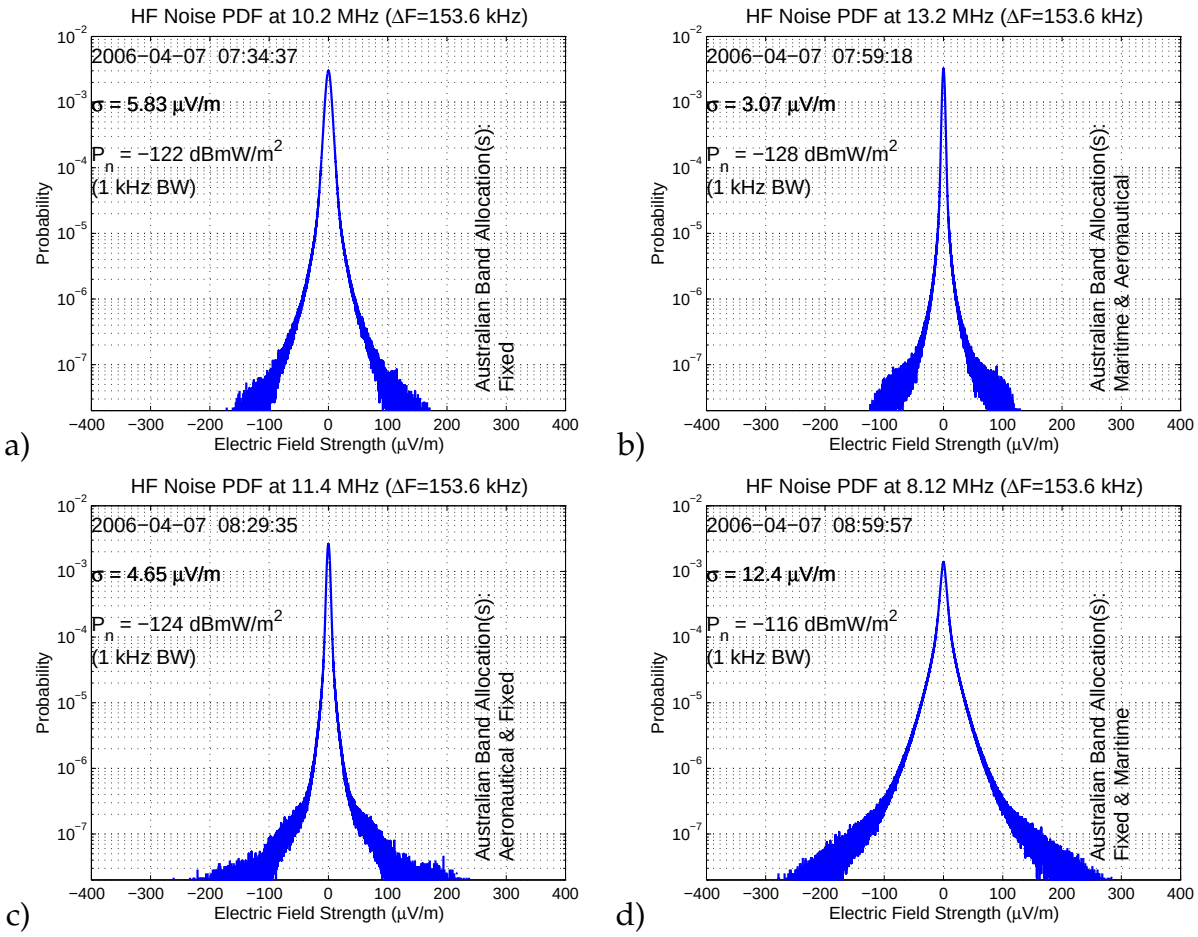


**Figure 7.7. The PDF of HF noise—07 April 2006, 07:30 hr to 09:30 hr local time.** Probability density functions for HF noise near Swan Reach, South Australia on 07 April 2006 from 07:30 hr to 09:30 hr local time. The timestamp for each PDF indicates the time at which a 30 min (nominal) data recording began. Note the Gaussian-like shoulders of sub-figures b) and c). The bandwidth of the data source is 153,600 Hz (a function of the design of the broadband receiver at Swan Reach) and the centre of the band is indicated in the title of the sub-figure. The band allocation (see Appendix F) indicates that the data for the PDF may contain signals corresponding to the listed band type(s). The variable $\sigma$ represents the RMS electric field strength in the 153.6 kHz bandwidth, and $P_{\mathrm{n}}$ is the noise power density (in a 1 kHz bandwidth) computed by Eq. (7.1).

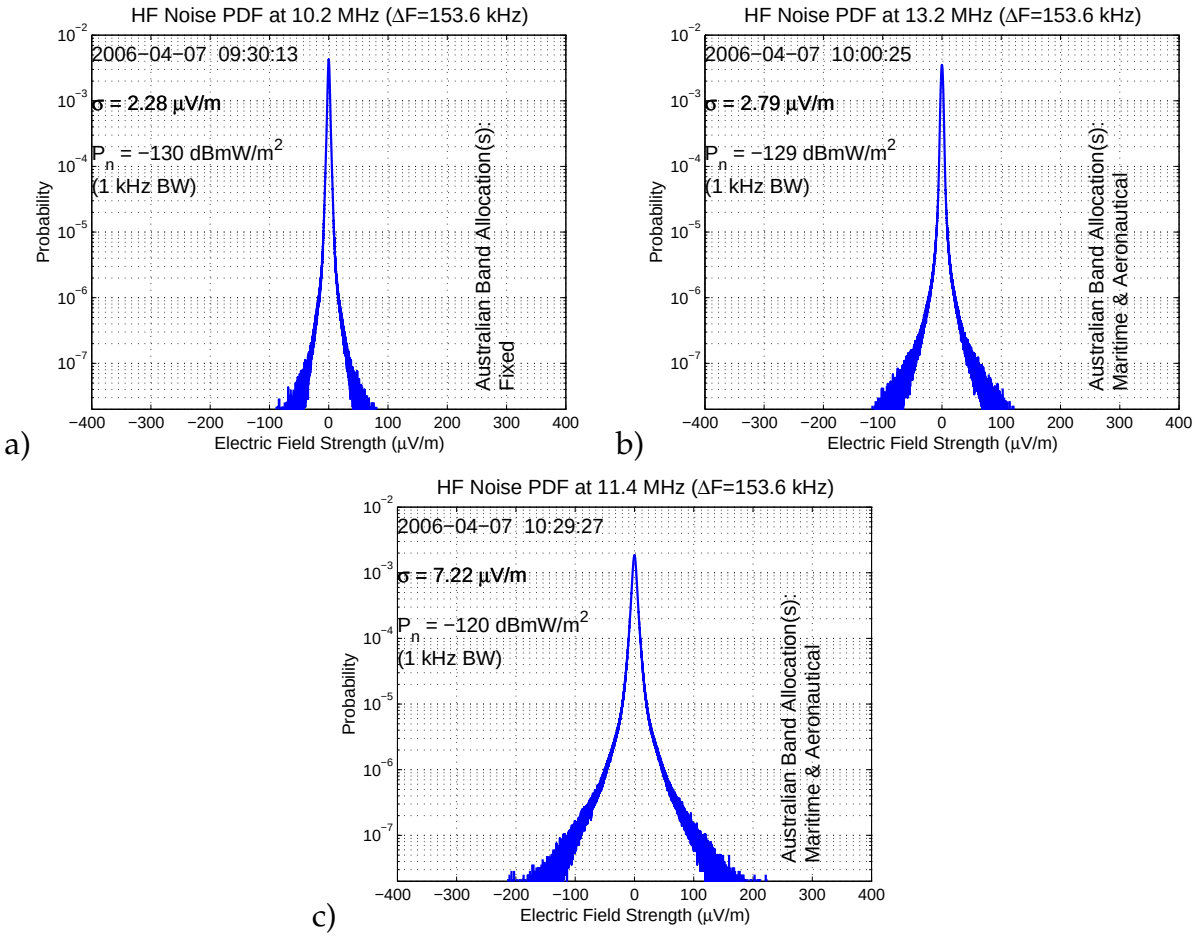


**Figure 7.8. The PDF of HF noise—07 April 2006, 09:30 hr to 11:00 hr local time.** Probability density functions for HF noise near Swan Reach, South Australia on 07 April 2006 from 09:30 hr to 11:00 hr local time. The timestamp for each PDF indicates the time at which a 30 min (nominal) data recording began. The bandwidth of the data source is 153,600 Hz (a function of the design of the broadband receiver at Swan Reach) and the centre of the band is indicated in the title of the sub-figure. The band allocation (see Appendix F) indicates that the data for the PDF may contain signals corresponding to the listed band type(s). The variable $\sigma$ represents the RMS electric field strength in the 153.6 kHz bandwidth, and $P_{\mathrm{n}}$ is the noise power density (in a 1 kHz bandwidth) computed by Eq. (7.1).

## Results from May 26, 2006

Figures 7.9 to 7.12 show more diversity than the previous figures. Figure 7.9 is benign in the sense that each PDF shows the expected peaked shape. Parts b) and d) may be showing a small Gaussian component at their shoulders. If so, it is likely due to weak signals bypassing the threshold detection in the broadband method. Note the timestamps in the sub-figures; all are pre-dawn. Prior to dawn, the D-region is not yet formed, and so distant and weak man-made signals in the congested aeronautical bands may possibly be contributing to the slightly rounded shoulders.

Gaussian components are more noticeable in Figure 7.10. In particular, sub-figures a), b), and c). However, as the timestamp increases with each sub-figure, the Gaussian component eventually becomes insignificant. This logic follows into Figure 7.11. There is a plausible explanation for this and it is the same as that for the results of the swept-narrowband method. During the hours of dawn, the D-region begins to form and as it does, it begins attenuating signals from distant locations. Simultaneously, environmental noise increases as human activities increase with the start of the day. However, as the D-region grows, it gradually gains the upper-hand and silences the distant man-made signals. Consequently, the Gaussian component reduces. Local groundwave interference does not appear to play a role. If it did, one would expect to see a Gaussian component in the PDF later in the day, as was seen in the results of the swept-narrowband method. Finally, it is worth noting that all of the sub-figures cover congested bands. Part b) covers a band, centred at 11.1 MHz, that appears particularly congested. The shoulders of the PDF are broad indicating significant human HF communications.

Figure 7.11 shows that as the day progresses, the Gaussian component in the previous figure disappears. It also illustrates, again, the impulsive nature of HF noise. Figure 7.12, however, is a stark contrast to the previous figures and therefore requires explanation.

The PDF in each sub-figure of Figure 7.12 is based on approximately 2 min of data collected with a running automobile engine near the antenna array. This engine is operated with the lead to one spark plug positioned so that arcing occurs between the lead and the engine block. It is well known that such arcing creates wideband noise,

not unlike that produced by lightning (Coleman 2006), and it is evident from the very strong Gaussian shapes. This *mini*-experiment also shows the effect of groundwave interference—it broadens the noise PDF.

Data collected on May 26, 2006 further suggests that the statistics of natural HF noise follow a peaked probability distribution. At times there may be a Gaussian component to the distribution, but the general shape remains impulsive.

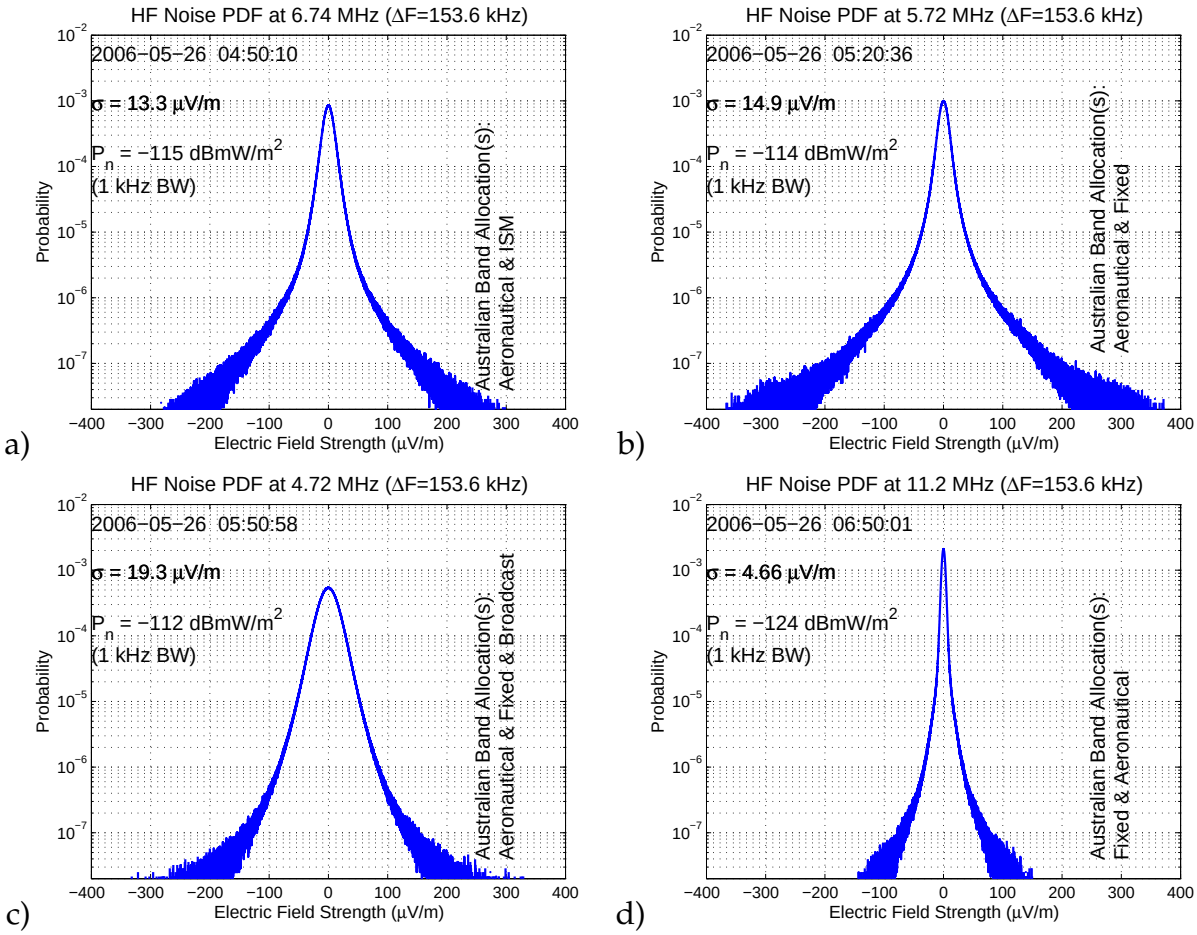


**Figure 7.9. The PDF of HF noise—26 May 2006, 04:50 hr to 07:20 hr local time.** Probability density functions for HF noise near Swan Reach, South Australia on 26 May 2006, 04:50 hr to 07:20 hr local time. The timestamp for each PDF indicates the time at which a 30 min (nominal) data recording began. The bandwidth of the data source is 153,600 Hz (a function of the design of the broadband receiver at Swan Reach) and the centre of the band is indicated in the title of the sub-figure. The band allocation (see Appendix F) indicates that the data for the PDF may contain signals corresponding to the listed band type(s). The variable $\sigma$ represents the RMS electric field strength in the 153.6 kHz bandwidth, and $P_n$ is the noise power density (in a 1 kHz bandwidth) computed by Eq. (7.1).

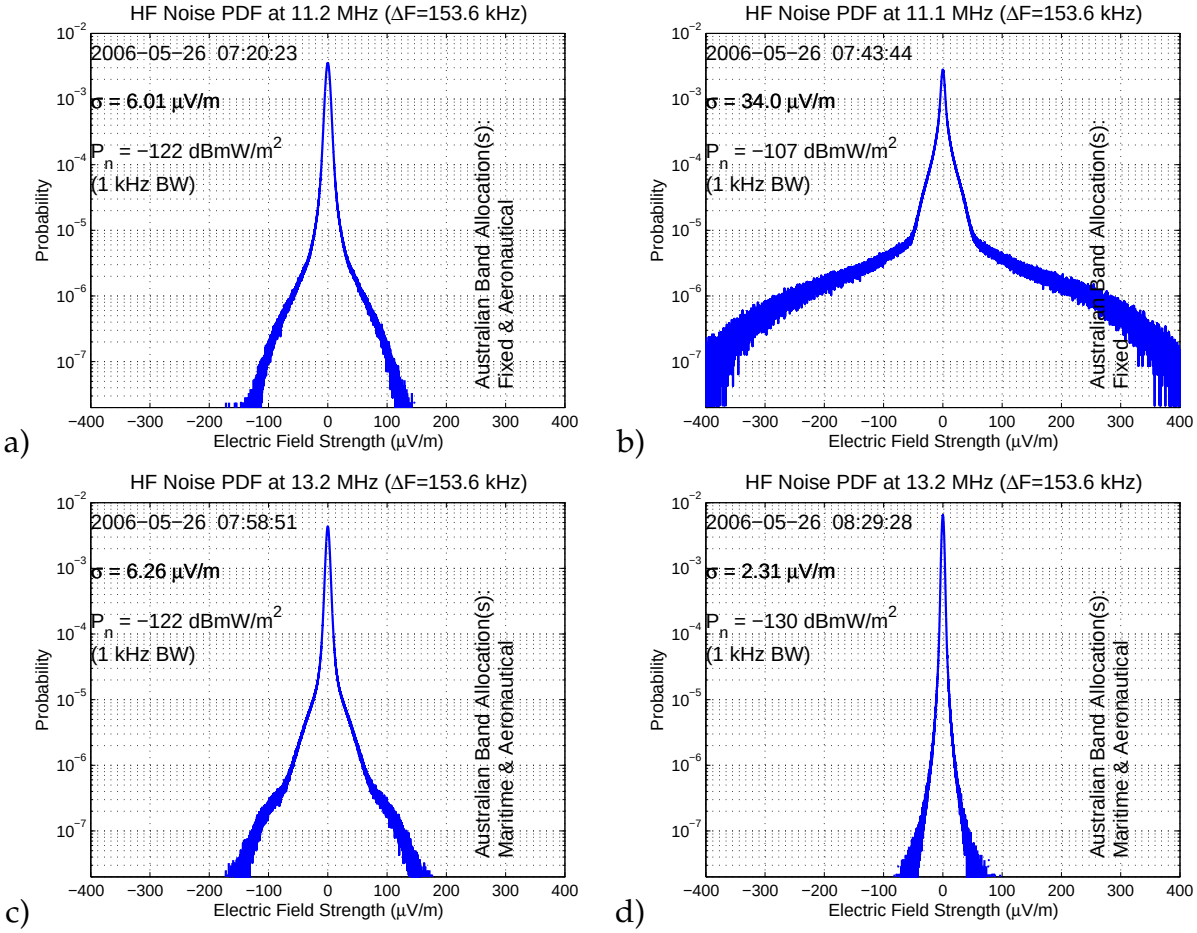


**Figure 7.10. The PDF of HF noise—26 May 2006, 07:20 hr to 08:45 hr local time.** Probability density functions for HF noise near Swan Reach, South Australia on 26 May 2006, 07:20 hr to 08:45 hr local time. The timestamp for each PDF indicates the time at which a 30 min (nominal) data recording began. However, subfigure a) is based on approximately 23 min of data and subfigure b) 15 min (see Appendix B for more information). The bandwidth of the data source is 153,600 Hz (a function of the design of the broadband receiver at Swan Reach) and the centre of the band is indicated in the title of the sub-figure. The band allocation (see Appendix F) indicates that the data for the PDF may contain signals corresponding to the listed band type(s). The variable $\sigma$ represents the RMS electric field strength in the 153.6 kHz bandwidth, and $P_{\mathrm{n}}$ is the noise power density (in a 1 kHz bandwidth) computed by Eq. (7.1).

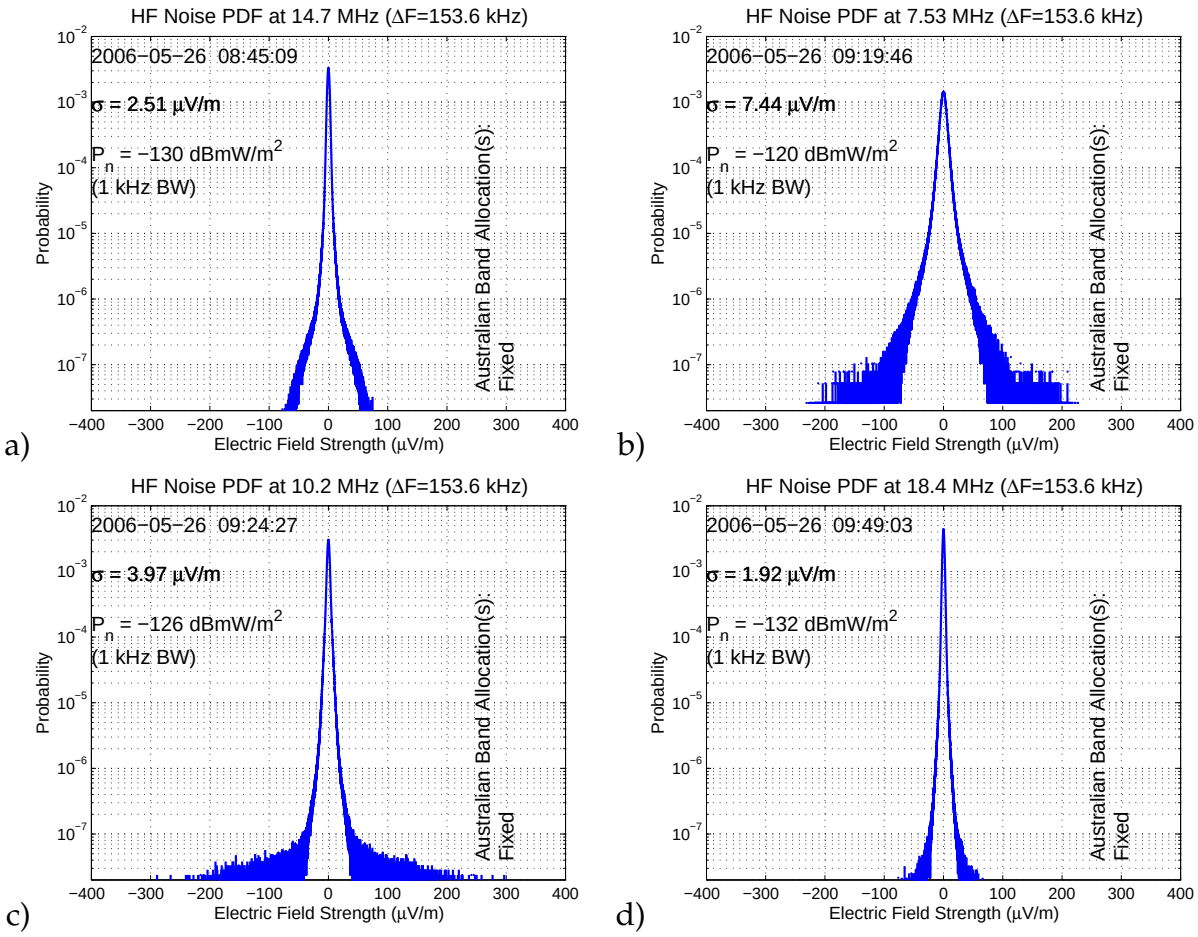


**Figure 7.11. The PDF of HF noise—26 May 2006, 08:45 hr to 10:20 hr local time.** Probability density functions for HF noise near Swan Reach, South Australia on 26 May 2006, 08:45 hr to 10:20 hr local time. The timestamp for each PDF indicates the time at which a 30 min (nominal) data recording began. The bandwidth of the data source is 153,600 Hz (a function of the design of the broadband receiver at Swan Reach) and the centre of the band is indicated in the title of the sub-figure. The band allocation (see Appendix F) indicates that the data for the PDF may contain signals corresponding to the listed band type(s). The variable $\sigma$ represents the RMS electric field strength in the 153.6 kHz bandwidth, and $P_\mathrm{n}$ is the noise power density (in a 1 kHz bandwidth) computed by Eq. (7.1).

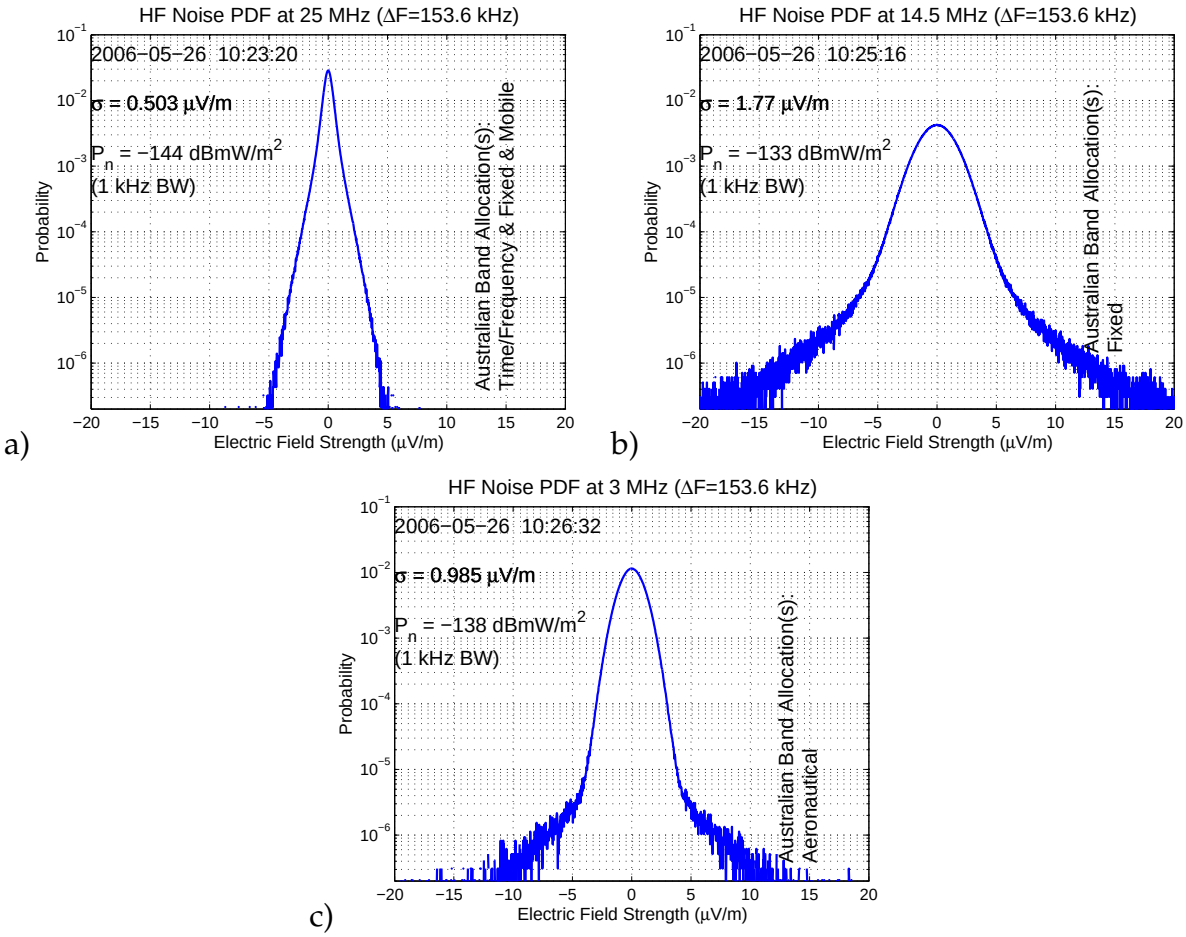


**Figure 7.12. The PDF of HF noise—26 May 2006, 10:20 hr to 10:30 hr local time.** Probability density functions for HF noise plus car ignition noise near Swan Reach, South Australia on 26 May 2006, 10:20 hr to 10:30 hr local time. The timestamp for each PDF indicates the time at which a 2 min (approximate) data recording began. During each recording, an automobile engine was operated near the antenna array. One spark plug lead was position against the engine block in a way that would allow arcing to occur. The arcing broadens the PDF and adds a strong Gaussian component to the PDF. The bandwidth of the data source is 153,600 Hz (a function of the design of the broadband receiver at Swan Reach) and the centre of the band is indicated in the title of the sub-figure. The band allocation (see Appendix F) indicates that the data for the PDF may contain signals corresponding to the listed band type(s). The variable $\sigma$ represents the RMS electric field strength in the 153.6 kHz bandwidth, and $P_{\mathrm{n}}$ is the noise power density (in a 1 kHz bandwidth) computed by Eq. (7.1).

## 7.4 The Effect of the Noise Threshold on the PDF

Both noise measurement techniques (*i.e.* swept-narrowband and broadband) require that a threshold be set to distinguish man-made signals from natural HF noise. The methods assume that HF energy above this threshold is man-made while HF energy below this threshold is natural HF noise (see Sections 5.2 and 5.3). The threshold for the swept-narrowband method is $L_p = 6\%$ and the broadband method uses a threshold of $L_p = 3\%$. These thresholds are chosen based on the visual structure of the data, but that very choice raises a question: what effect does the choice of $L_p$ have on the PDF?

To observe the effect, take for example, the data set collected on 7 April 2006 at 8:59am local time (GMT+9:30) and recompute the PDF (using the broadband method) at thresholds of 3%, 5%, 10%, 15%, 20%, and 25%. One would expect that as the threshold increases the proportion of man-made signals in the PDF would increase, thereby causing the PDF to appear less impulsive in nature. Indeed, Figure 7.13 shows that this is the case.

It is obvious that the choice of threshold does affect the PDF. However, in this data set the effect is not significant until the threshold exceeds about 10%. The threshold for which the PDF deviates significantly from the impulsive structure will depend on frequency since the level of noise varies approximately inversely with frequency. No matter what frequency, a threshold that is too low will cause man-made and some natural HF noise to be excluded from the analysis (resulting in a particularly impulsive PDF). If it is too high, natural HF noise and some man-made noise will be included in the analysis (resulting in a Gaussian-like PDF).

A review of Figures 7.2 to 7.12 suggests that, in general, below about 8 MHz the PDF broadens significantly in comparison to the PDF above 8 MHz, which implies that the threshold is too high for the frequencies below 8 MHz and probably too low for the higher frequencies. This apparent contradiction with the logic above may be explained by the fact that the minimum sunspot conditions tend to encourage propagation of HF signals at low frequencies. As a result, the man-made noise at the high frequencies is low relative to the man-made noise at low frequencies and therefore the PDF at the high frequencies still appears impulsive, while the PDF at the low frequencies appears to have a Gaussian component. The threshold at the high frequencies is therefore too

high despite the lack of an observable Gaussian component in the PDF, and the threshold at the low frequencies is also too high for the propagation conditions.

For these reasons one can say that the assumption of 3% for the broadband method and 6% for the swept-narrowband method is reasonable for excising man-made signals from the data sets presented. In addition, the PDF of natural HF noise is non-Gaussian and impulsive.

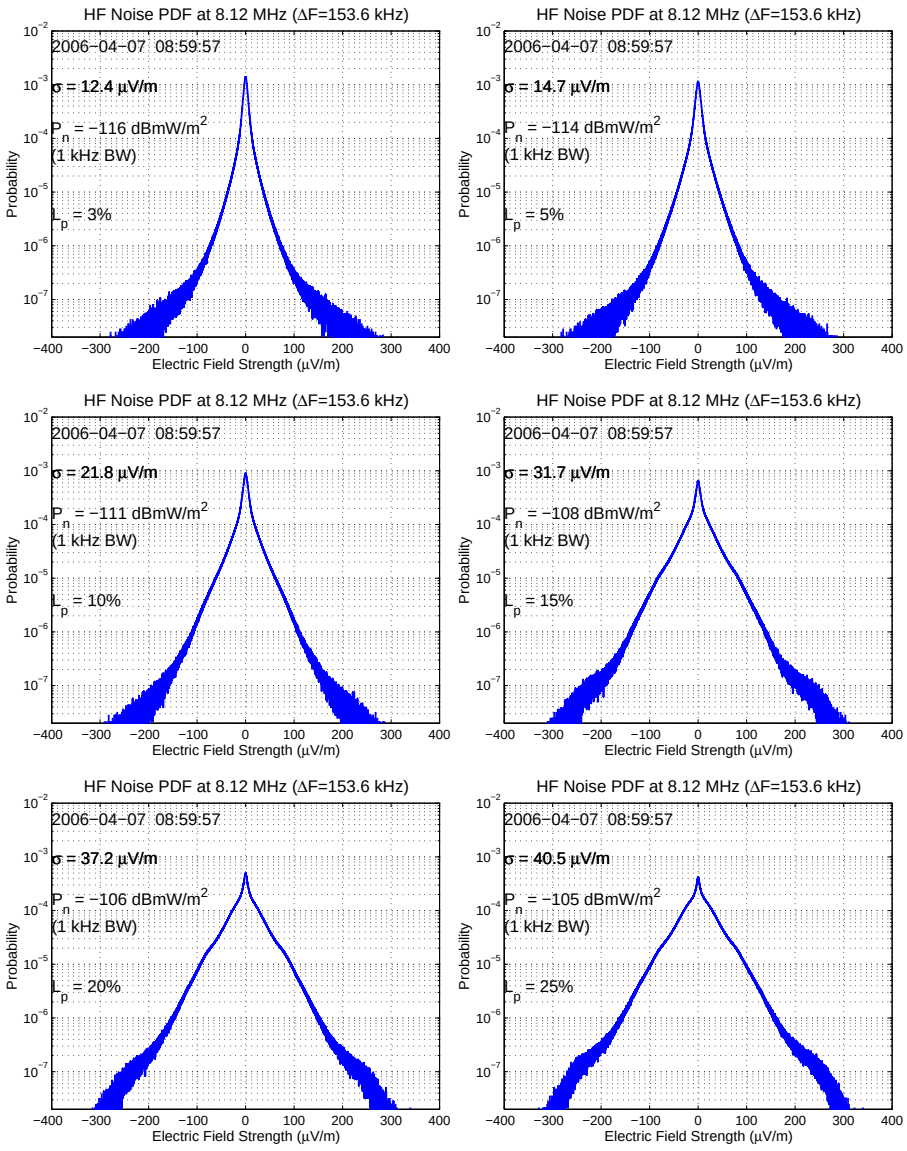


**Figure 7.13. The effect of the threshold on the shape of the noise PDF.** The effect of the threshold on the probability density function for HF noise near Swan Reach, South Australia on 7 April 2006, 09:00 hr to 09:30 hr local time. The timestamp of 08:59:57 indicates the time at which a 30 min (nominal) data recording began. The bandwidth of the data source is 153,600 Hz (a function of the design of the broadband receiver at Swan Reach) and the centre of the band is 8.12 MHz. The variable $\sigma$ represents the RMS electric field strength in the 153.6 kHz bandwidth, and $P_{\mathrm{n}}$ is the noise power density (in a 1 kHz bandwidth) computed by Eq. (7.1). Each subfigure is computed with a different value of $L_p \in \{3\%, 5\%, 10\%, 15\%, 20\%, 25\%\}$. As the value of $L_p$ increases, the shape of the PDF broadens with increasingly Gaussian-like shoulders, which suggests that a high threshold allows a greater proportion of man-made signals to corrupt the PDF.

## 7.5 Bi-Kappa Fit to Data Sets

The results in the previous sections strongly suggest that the PDF of natural HF noise is not Gaussian. So, what distribution does it resemble?

Ibukun (1966) discusses a variety of lognormal distributions to model HF atmospheric noise. One such distribution that describes the probability that the noise voltage envelope exceeds a threshold is defined as

$$Q(v) = \left[1 + \left(\frac{\alpha v}{\widehat{v}}\right)^{r}\right]^{-1}, \tag{7.2}$$

where $v$ is the noise voltage threshold, $\widehat{v}$ is the average envelope voltage of the noise, and $\alpha$ and $r$ are tuning factors. Nakai (1960) uses this distribution and models the noise in Japan with $\alpha = 2.7$ and $r = 1.4$. With such values for $\alpha$ and $r$, and various $\widehat{v}$, Eq. (7.2) appears as shown in Figure 7.14. Note that Eq. (7.2) is not normalized to the area under the curve.

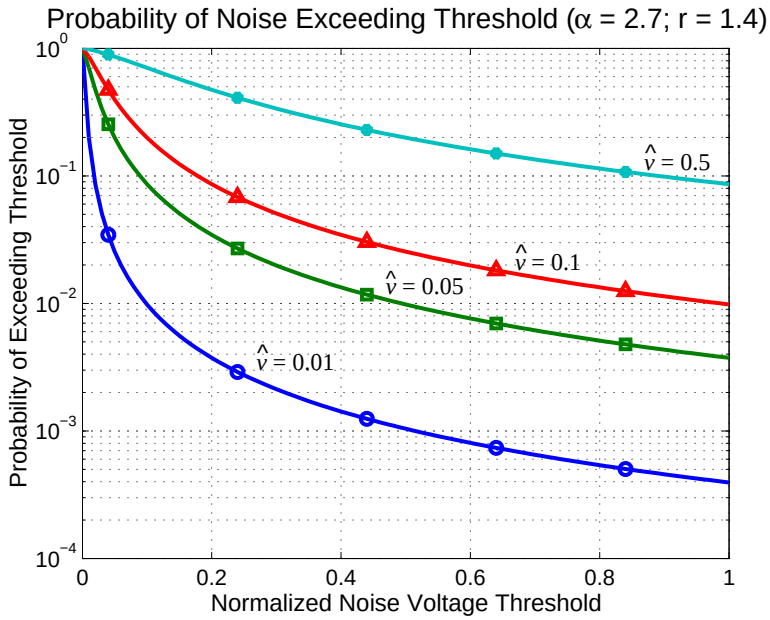


**Figure 7.14. A lognormal model for the PDF of atmospheric HF noise in Japan.** This early lognormal model for the PDF of atmospheric HF noise is referenced by Ibukun (1966) and described by Eq. (7.2). At the time of Ibukun's paper (1966), the distribution had no physical justification and so Nakai's (1960) choice of the tuning parameters, $\alpha = 2.7$ and $r = 1.4$, are somewhat arbitrary in his modeling of atmospheric HF noise in Japan. The effect of varying the average envelope voltage, $\widehat{v}$ is also shown. Note the peaked shape of the distribution centred near the origin, particularly for low $\widehat{v}$.

However, in 1966 (the year of Ibukun's paper), Ibukun admits that a physical justification for the lognormal distribution does not exist. Yet, the distribution is strikingly similar to the Bi-Kappa distribution presented by Leubner & Vörös (2005) to describe the probability distribution of the solar wind.

The Bi-Kappa distribution is the superposition of two distributions, a so-called *halo* distribution and a *core* distribution, such that

$$p(\delta\mathbf{X};\kappa) = \frac{1}{2\sqrt{\pi}\sigma}\left\{\left[1+\frac{\delta\mathbf{X}^2}{\kappa\sigma^2}\right]^{-\kappa} + \left[1-\frac{\delta\mathbf{X}^2}{\kappa\sigma^2}\right]^{\kappa}\right\}, \tag{7.3}$$

where $\delta\mathbf{X}(\tau) = X(t+\tau) - X(t)$ and where $X(t)$ is any physical random variable in the nonextensive system of interest, $\tau$ is a time lag that characterizes the separation scale of the physical variable (*e.g.* for solar wind $\tau$ measures the spatial separation in terms of units of time[21]), and $\sigma$ is the variance of the physical variable. The nonextensivity parameter, $\kappa$, represents a measure of long-range interactions. The term *nonextensive* is often used to describe systems that do not have strong dependencies on initial conditions, whereas an *extensive* system (*e.g.* one described by Boltzmann-Gibbs extensive thermo-statistics) is dependent on initial conditions. In the context of HF noise, $\kappa$ measures the influence of local man-made noise sources versus near and distant natural noise sources (*e.g.* lightning).

Whereas, Leubner and Vörös interpret $X(t)$ as the speed of the solar wind and $\tau$ as a measure of the spatial scale of the astrophysical system, for this discussion $X(t)$ refers to the electric field strength in units of $\mu$V/m at time $t$ and $\tau$ as only a time delay. It is acknowledged that the HF noise distribution at any point in time and at any geographical location is a result of noise fluctuations over a space-time domain. For the most part, this domain is dominated by the fluctuations from atmospheric noise sources and less so from cosmic radiators. Unlike the tens of astronomical units[22] assumed by Leubner and Vörös, this work assumes that distances between local and long-range noise sources are constrained by the dimensions of the earth. This means

[21] This is a sensible statement since long-range (or distant) forces affect the solar wind some time after the observation time, $t$, because of the distance.

[22] One astronomical unit is equivalent to the distance between the earth and the sun.

that long-range noise sources can propagate in a fraction of a second to the geographical observation point. Consequently, $\tau$ in Eq. (7.3) has no real meaning as a measure of spatial scale in the context of HF noise from natural sources and therefore $\delta\mathbf{X}$ should rightly be replaced by $X(t)$.

As already mentioned, the two terms in Eq. (7.3) represent *halo-core* structures in nonextensive astrophysical environments. The first term is the *halo* component and the second term is the *core* component. Either component is suitable for the present discussion. If the *halo* component,

$$f_{\mathrm{h}} = \frac{1}{2\sqrt{\pi}\sigma}\left[1+\frac{X^2}{\kappa\sigma^2}\right]^{-\kappa}, \tag{7.4}$$

is used $\kappa$ must be positive definite. If the alternative *core* component,

$$f_{\mathrm{c}} = \frac{1}{2\sqrt{\pi}\sigma}\left[1-\frac{X^2}{\kappa\sigma^2}\right]^{\kappa}, \tag{7.5}$$

is used $\kappa$ must be negative definite. Notice also that the *core* component is the same as the *halo* term for this condition. So for this work, a modified Bi-Kappa distribution is defined (see Appendix A.1) as

$$p(X;\kappa) = \frac{1}{\sigma\sqrt{\kappa}\beta(\frac{1}{2},\kappa-\frac{1}{2})}\left(1+\frac{X^2}{\kappa\sigma^2}\right)^{-\kappa} \quad \kappa > \tfrac{1}{2}, -\infty < X < +\infty, \tag{7.6}$$

or for finite $X$,

$$p(X;\kappa) = \frac{1}{F(b)-F(a)}\left(1+\frac{X^2}{\kappa\sigma^2}\right)^{-\kappa} \quad \kappa > \tfrac{1}{2}, a < X < b, \tag{7.7}$$

where $F(z)$ is the cumulative distribution function of Eq. (7.6) evaluated at $z \in \mathbb{R}$. An easy method to determine $F(b) - F(a)$ is to calculate the area under the probability curve.

What Eq. (7.6) means is that with a single parameter, $\kappa$, the level of natural HF noise and man-made noise in the model can be controlled. As $\kappa \to \infty$, Eq. (7.6) approaches a Gaussian, which can suggest strong interactions from local man-made noise sources.

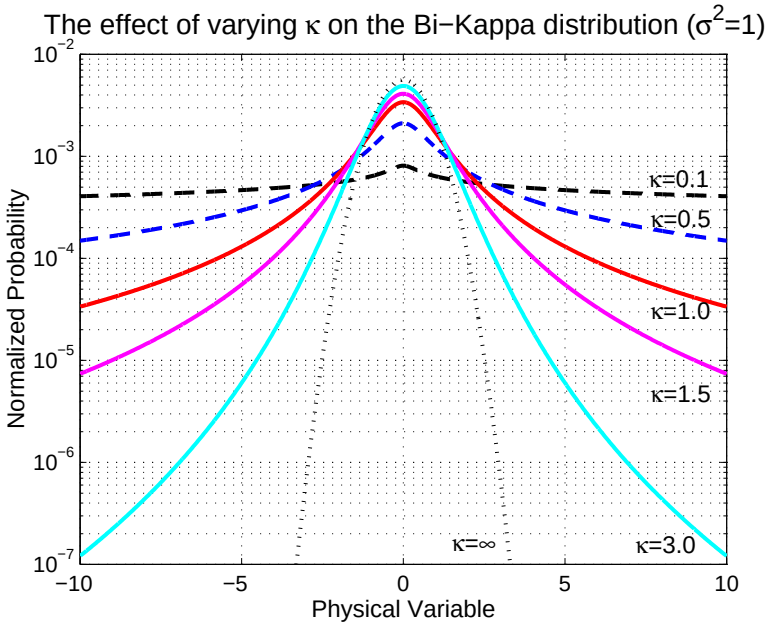


**Figure 7.15. The effect of $\kappa$ on the modified Bi-Kappa distribution.** The effect of varying $\kappa$ of the modified Bi-Kappa distribution is to cause a change from a Gaussian distribution at $\kappa = \infty$ (dotted black curve), to a peaked distribution with long tails for $\frac{1}{2} < \kappa << \infty$, to finally a uniform distribution at $\kappa = 0$. The limit on $\kappa$ (indicated by the dashed blue curve) is dictated by the formulation of the normalizing constant. If the normalization constant is ignored the range of $\kappa$ can be extended so that $0 \leq \kappa < \infty$. In this example, the distributions have unity variance, which accounts for the broadness of the peak. Decreasing the variance produces a sharper peak.

On the other hand, as $\kappa$ decreases from $\infty$, Eq. (7.6) tends to become impulsive or intermittent, which indicates strong contributions from natural noise sources (*e.g.* lightning). The effect of $\kappa$ on the distribution is shown in Figure 7.15.

So with this in mind, the focus returns to the fitting of the observed distributions. In the mid-20$^{th}$ century Clarke (1962), Ibukun (1964, 1966), and others (Aiya 1962, Hoff & Johnson 1952, Furutsu & Ishida 1961, Yuhara *et al* 1956, Nakai 1960, Likhter Ya 1956, Foldes 1960) reported on the non-Gaussian structure of natural HF noise. Johnson *et al* (1997) also reports that HF noise cannot be modeled as Gaussian, but rather consists of impulses of significant amplitude that have diurnal, seasonal, and geographical variations. During evening and night hours, the noise PDF is predominantly non-Gaussian, that is, impulsive. During the morning and daylight hours, especially near urban areas, the dominant component of HF noise is man-made. To illustrate this behaviour,

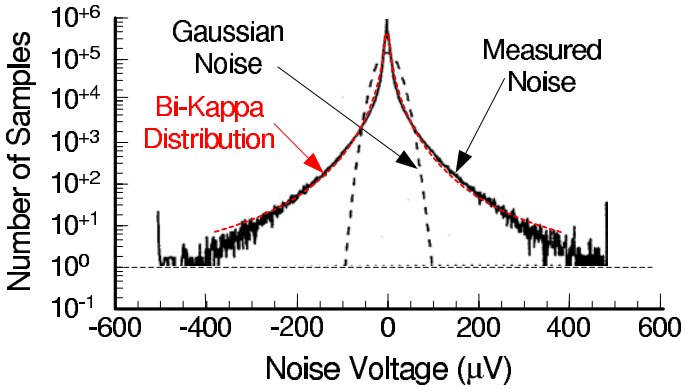


**Figure 7.16. The PDF of HF noise from Johnson.** Johnson *et al* (1997) describes HF noise as impulsive, having diurnal, seasonal, and geographical variations. This PDF of HF noise voltage, adapted from Johnson, is at a frequency of 5.4765 MHz in the Australian region. Johnson does not report the timeframe of the measurement, nor the units of noise voltage. Units of $\mu$V are therefore assumed for the noise voltage. A Gaussian PDF of the same noise power as the measured noise is overlaid on the graph. The Bi-Kappa distribution (in red) has a standard deviation, $\sigma = 14.5$ $\mu$V, and an extensivity factor, $\kappa = 0.92$.

Figure 7.16 is adapted from Johnson, but is also overlaid with a distribution defined by Eq. (7.7).

Clearly, the noise PDF that Johnson presents also has a Bi-Kappa distribution, not unlike that of Figure 7.17, which fits the Bi-Kappa distribution to two PDFs of Figure 7.1. Both Figures 7.16 and 7.17, show that natural HF noise is not Gaussian. Of note is the predominance of low-amplitude noise impulses and the high probability of high-amplitude noise excursions.

The Bi-Kappa distribution fits the results of the broadband method closely. Figure 7.18 contains four examples. Sub-figures a) and b) are from the 6–7 April 2006 data set and sub-figures c) and d) are from the 26 May 2006 data set. Each shows good correlation between measured values and the fitted Bi-Kappa distribution.

In fact, the shape of the measured noise at Swan Reach more closely resembles Figure 7.16 than the shape of the noise measured in Adelaide. This is not due to the differences in the methods (*c.f.* broadband method and swept-narrowband method), but rather it is due to the level of man-made noise at the two sites. At Swan Reach the level of man-made noise is relatively low compared to the man-made noise in Adelaide.

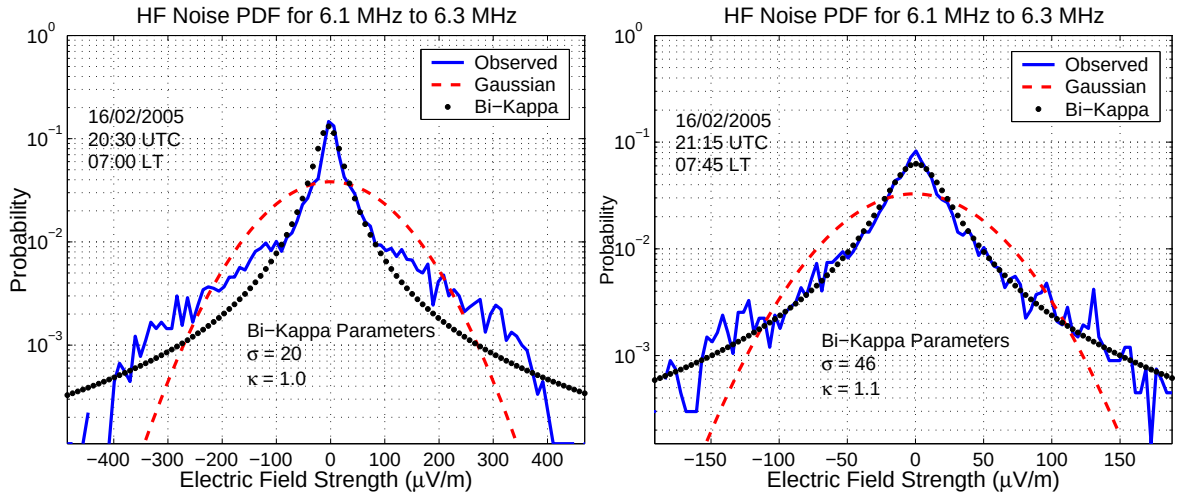


**Figure 7.17. Bi-Kappa fit to the HF noise PDF.** Fit of a Bi-Kappa distribution (dotted curve) and Gaussian distribution (dashed curve) to the PDF of HF noise in a 4 kHz band at 07:00 hr (*left*) and 07:45 hr (*right*). For the 7:00 am observation the measured standard deviation is 100 $\mu$V/m, while $\sigma = 20$ $\mu$V/m for the Bi-Kappa distribution. In this case the Bi-Kappa distribution fits the observed PDF in the range of $-100$ $\mu$V/m to 100 $\mu$V/m. At 7:45am, the Bi-Kappa distribution fits much better. Here $\sigma = 46$ $\mu$V/m for the Bi-Kappa distribution, and is the same as the measured standard deviation (46 $\mu$V/m).

Figure 7.18 shows that at Swan Reach there is a high probability of low-level HF noise, and a significant probability that the envelope of the noise will have large excursions about its mean. All of this suggests that the noise is bursty and impulsive, which agrees with Johnson *et al* (1997) and others (Coleman 2006, Maslin 1987).

## 7.6 Noise versus Frequency

So far, the discussion has concentrated on the shape of the natural HF noise PDF. The data, however, also provides some indication of the variation of the noise with frequency and time of day. Figure 7.19 contains the RMS noise electric field strength ($\mu$V/m) from Figures 7.2 to 7.11 at the corresponding centre frequencies at different times of day. Measurements from Figure 7.12 are excluded because of contamination by ignition noise. The anomalous measurement from Figure 7.10b is also excluded.

Figure 7.19 immediately conveys two observations. The first is that the strength of the noise decays with frequency in an $1/f$ fashion. It is well known that HF noise follows

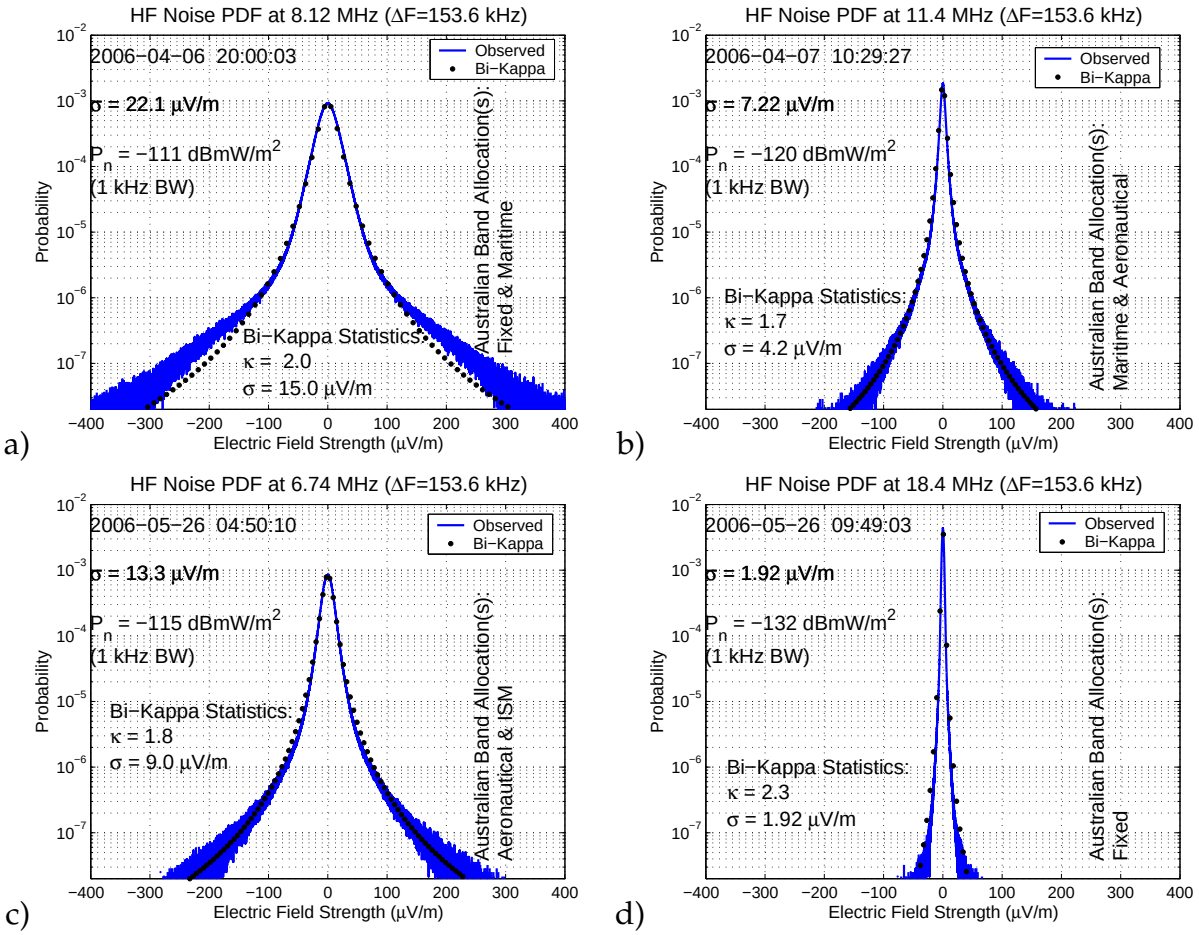


**Figure 7.18. Fit of Bi-Kappa Distribution to Swan Reach data.** Fit of Bi-Kappa distribution to the PDF of the measured HF noise near Swan Reach, South Australia. Four different local times are chosen to illustrate that the Bi-Kappa distribution is a reasonable fit to the PDF of HF noise. Sub-figures a) and b) are from the 6–7 April data set respectively. Sub-figures c) and d) are from the 26 May data set. The timestamp for each PDF indicates the time at which a 30 min (nominal) data recording began. The bandwidth of the data source is 153,600 Hz (a function of the design of the broadband receiver at Swan Reach) and the centre of the band is indicated in the title of the sub-figure. The band allocation (see Appendix F) indicates that the data for the PDF may contain signals corresponding to the listed band type(s). The variable $\sigma$ represents the RMS electric field strength in the 153.6 kHz bandwidth, and $P_{\mathrm{n}}$ is the noise power density (in a 1 kHz bandwidth) computed by Eq. (7.1). Under the heading, "Bi-Kappa Statistics", are the tuning parameter, $\kappa$, and standard deviation for the fitted Bi-Kappa distribution.

such a relationship (CCIR 1986, Johnson *et al* 1997, IPS Radio and Space Services 1994). Secondly, noise levels in the evening (1700 hr to 2400 hr local time) are stronger than earlier in the day. At night the D-region of the ionosphere is nearly non-existent and

therefore noise from distant sources is more easily received by the broadband receivers at Swan Reach. Measurements made in the morning daylight hours appears slightly stronger than those of the pre-dawn and dawn hours, which is consistent with increased environmental noise during the day due to human activity.

The RMS noise strength measurements are summarized in Figure 7.20, where each column of samples in Figure 7.19 are averaged to yield a single point. A $1/f$ curve is shown for reference, but a curve following a $1/f^{1.45}$ appears to fit the data better.

Finally, it must be emphasized that the sun is currently at sunspot minimum conditions and so communications at frequencies above approximately 10 MHz is difficult. In addition, noise sources above 10 MHz contribute less to the HF noise PDF than would be the case during sunspot maximum conditions. It is well known (IPS Radio and Space Services 1994) that with increasing sunspot number there is increasing electron density in the ionosphere, and a corresponding increase in the maximum useable frequency (MUF)[23]. A highly ionized ionosphere therefore accommodates skywave propagation of signals and noise over a broader range of frequencies. During sunspot maximum conditions, the noise levels would therefore be greater than those measured here.

## 7.7 Other Supporting Evidence

During testing of the broadband receiver, Ebor Computing took measurements of the ambient HF noise near Swan Reach, in June–July 2006. The measurements were conducted with a Rohde & Schwarz noise test set with a calibrated antenna. These measurements show that the ambient HF electric field strength (vertical component) in a 1 kHz band varies greatly from about -15 dB$\mu$V/m (0.031 $\mu$V/m) to approximately +5 dB$\mu$V/m (3.16 $\mu$V/m). Within an order of magnitude these measurements support the correctness of the scaling applied by the broadband method to the April–May 2006 data sets. In other words, the RMS electric field strength quoted in Figures 7.2–7.12 are comparable to the levels determined by Ebor Computing.

As a further check, the ITU report (CCIR 1986) on atmospheric radio noise contains a method to predict the noise field strength. To begin, the median effective antenna

[23]The MUF is the highest frequency that will reliably support communications via skywave propagation.

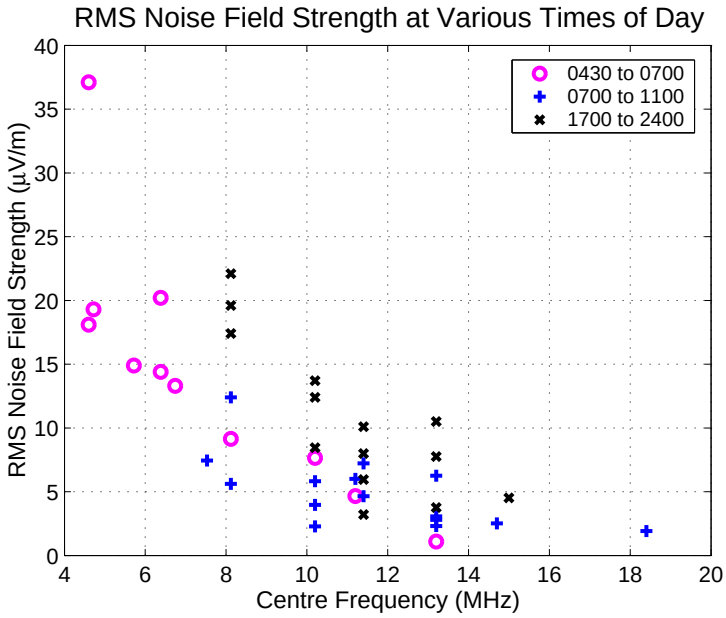


**Figure 7.19. Measured noise levels throughout the day.** The measured RMS noise field strengths from the Swan Reach data set are shown here. A vertical column of samples represent measurements taken Figures 7.2 to 7.11 at a particular frequency at different times of day. Measurements from Figure 7.12 are excluded because of contamination by ignition noise. The anomalous measurement from Figure 7.10b is also excluded. Two observations that are immediately apparent are that the noise field strength follows a $1/f$ curve (see Figure 7.20) and that the noise in the evening (1700 hr to 2400 hr local time) is stronger than earlier in the day. Intuitively this is correct since the D-region of the ionosphere is nearly non-existent at night and noise from distant locations is no longer attenuated as greatly as during the day. Measurements made in the morning daylight hours appears slightly stronger than those of the pre-dawn and dawn hours, which is consistent with increased environmental noise during the day due to human activity.

noise figure (dB) is obtained from the charts in the report for the season (*i.e.* in this case autumn) and time of day. Then Eq. (5.5) is used with $F_a$ set to the median noise figure, $F_{\text{MHz}}$ set to the centre frequency of the bandwidth, and $b$ set to 153.6 kHz. Doing so produces Table 7.7. Generally, the measured noise is within an acceptable 10 dB of the predicted noise. This provides further support for the validity of the swept-narrowband and broadband methods. Appendix D contains more detailed tables of predicted and measured noise strengths.

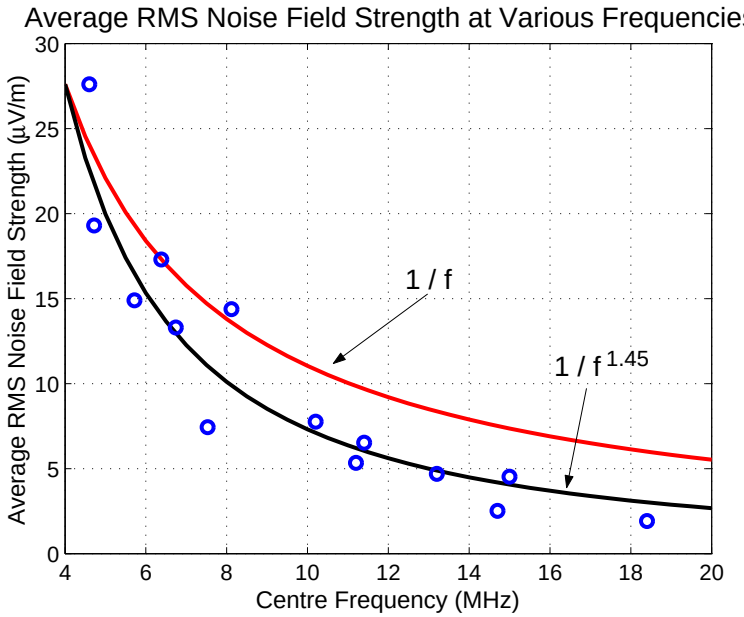


**Figure 7.20. Measured noise levels versus frequency.** The average RMS noise field strengths from the Swan Reach data set follow an inverse relationship with frequency. It is well published that HF noise follows such a curve (CCIR 1986, Johnson *et al* 1997, IPS Radio and Space Services 1994). Each sample point represents the average RMS noise field strength ($\mu$V/m) calculated by averaging the RMS electric field strengths from Figures 7.2 to 7.11 for specific centre frequencies (see Figure 7.19). Measurements from Figure 7.12 are excluded because of contamination by ignition noise. The anomalous measurement from Figure 7.10b is also excluded. A $1/f$ curve is shown, but the data is better approximated by a $1/f^{1.45}$ curve.

**Table 7.1. Comparison of ITU predicted noise levels and measured noise levels.** The ITU report (CCIR 1986) on atmospheric noise predicts the natural HF noise level at any location on earth. The procedure involves estimating the effective antenna noise figure of a lossless short vertical antenna over a perfectly conducting ground plane and then applying Eq. (5.5) to predict the RMS noise field strength in units of dB$\mu$V/m. These predictions are tabulated under the Predicted (Pred.) column. The Measured (Meas.) column is the average of all the measured noise field strengths for a particular time period and frequency, in units of dB$\mu$V/m from Figures 7.2 to 7.11. The anomalous RMS noise field strength from Figure 7.10b is not included in averages of the Measured column. For both the Predicted and Measured columns the noise bandwidth is 153.6 kHz. The full table is included for reference in Appendix D.

| **Centre Freq.** (MHz) | **Natural HF Noise Level** (dB$\mu$V/m) | | | | | | | |
|---|---|---|---|---|---|---|---|---|
| | Pred. (0400 hr – 0800 hr) | Meas. | Pred. (0800 hr – 1200 hr) | Meas. | Pred. (1600 hr – 2000 hr) | Meas. | Pred. (2000 hr – 2400 hr) | Meas. |
| 4.60 | 16.62 | 28.27 | | | | | | |
| 4.72 | 16.84 | 25.71 | | | | | | |
| 5.72 | 16.51 | 23.46 | | | | | | |
| 6.38 | 16.46 | 24.64 | | | | | | |
| 6.74 | 15.94 | 22.48 | | | | | | |
| 7.53 | | | -0.10 | 17.43 | | | | |
| 8.12 | 13.56 | 17.10 | 1.56 | 21.87 | 14.56 | 25.85 | 19.56 | 25.85 |
| 10.20 | 10.54 | 16.50 | 4.54 | 9.57 | 13.54 | 22.73 | 16.54 | 20.20 |
| 11.10 | 7.27 | 30.63 | | | | | | |
| 11.20 | 7.35 | 14.47 | | | | | | |
| 11.40 | | | 4.50 | 15.26 | 12.50 | 19.07 | 13.50 | 12.82 |
| 13.20 | 5.78 | 0.75 | 4.78 | 10.46 | 11.78 | 19.11 | 10.78 | 11.50 |
| 14.70 | | | 4.71 | 7.99 | | | | |
| 15.00 | | | | | 7.89 | 13.10 | | |
| 18.40 | | | -3.34 | 5.67 | | | | |

## 7.8 Summary

This chapter discusses the probability density function of HF noise as determined by two methods: the swept-narrowband method, and the broadband method. The swept-narrowband method is applied to a data set from an industrial site in Adelaide, while the broadband method is applied to data sets from a remote country location near Swan Reach, South Australia.

The results of the swept-narrowband method show that the data set from Adelaide is affected by local man-made interference. Local interference (*i.e.* environmental noise) varies from weak at dawn to strong throughout the daylight working hours. This variation is primarily due to and coincides with human activity throughout the working day. In addition, during the day, the D-region attenuates much HF noise from distant locations. Hence, there is a Gaussian component to the noise PDF, at times dominant, in addition to the natural HF noise component that is impulsive.

The results of the Swan Reach measurements (using the broadband method) show no apparent strong Gaussian noise, rather they clearly show the impulsive nature of HF noise. This lack of a strong Gaussian component suggests two things: 1) the site near Swan Reach is quiet in a electromagnetic sense; and 2) the receiving system is externally noise limited at that site. This second point lends itself to a procedure (to be addressed shortly) for determining whether or not an HF receiving system is externally noise limited.

All the data sets (*i.e.* the Adelaide data set and the two Swan Reach data sets) show that the PDF of HF noise is generally not Gaussian. It appears to follow a Bi-Kappa or similar distribution, which is peaked and impulsive (see Figures 7.17, and 7.18). Moreover, the PDF has diurnal variations and is affected by man-made groundwave and skywave interference. Significant man-made interference tends to add a Gaussian component to the PDF. This Gaussian component is strong in urban areas and weaker in remote country locations.

The results of both analysis methods are affected by the choice of noise threshold. Increasing the threshold broadens the PDF and allows a greater proportion of man-made noise to contaminate the PDF. An analysis of one data set shows that at a noise threshold of 15% the shoulders of the PDF begin to look Gaussian.

The chapter also discusses the fitting of the Bi-Kappa distribution to the observed distributions, with supporting evidence provided by work from the mid-$20^{th}$ century (Clarke 1962, Ibukun 1964, Ibukun 1966) and by Johnson *et al* (1997). The tuning parameter, $\kappa$, of the distribution can be used to model the effect of man-made noise as well as natural HF noise. As $\kappa \rightarrow \pm\infty$ the distribution converges on a Gaussian indicating a strong man-made noise component. For $\kappa \ll \infty$, the distribution is impulsive with long tails.

The noise data sets also record, to a limited extent, the variations of noise with frequency. The analysis of the results of the broadband method reveal that the noise versus frequency profile follows the well-known $1/f$ curve for HF noise (CCIR 1986, Johnson *et al* 1997, IPS Radio and Space Services 1994). Further support for the swept-narrowband method and broadband method is achieved by comparing the measured average noise levels with noise levels measured by Ebor Computing and those predicted by the ITU (CCIR 1986). The measured noise levels are generally within 10 dB of ITU predicted levels and Ebor Computing's measurements.

A previous suggestion proposed that the HF noise PDF could be used to assess whether or not a receiving system is externally noise limited. If a noise PDF, measured using the procedures in Chapter 5, has a strong Gaussian component it implies that either the receiver is not externally noise limited; or the level of man-made noise at the receive site is high. However, if the PDF is generated from data collected by a receiving system at a known "quiet" site and the PDF has a Gaussian component, it very likely means that the receiving system, as configured during the test, is not externally noise limited across its entire receive bandwidth. Consequently, a procedure to determine whether a receiving system is externally or internally noise limited might be based on the following:

1. perform noise figure (NF) and gain calculations to indicate system performance;
2. collect data, over the band of interest, for significant lengths of time at a known quiet site;
3. generate the PDF using the method in Section 5.3; and

4. compare the resultant PDF with a Bi-Kappa distribution (or similar impulsive HF noise model).

This chapter covers only a few issues related to HF noise. There are many issues still to resolve. However, some conclusions can be drawn from the results presented here and more work proposed but, these are best left for the next chapter.

Chapter 8

# Conclusions & Further Work for Part II

THERE are many more questions about HF noise to be answered that have not been answered by the preceding chapters. Indeed even the literature review in Chapter 4 raises unanswered questions. The purpose of this chapter is to summarize and make conclusions about the work in Part II of the thesis, and to highlight additional work that would extend the understanding of HF noise and form a basis for a useful noise model.

The impetus for investigating the probability density function of HF noise arose from the requirement for a better noise model for automatic modulation recognition techniques. Many current modulation recognition methods still assume Gaussian noise models for the noise injected by the transmission medium. For HF communications this can be an incorrect assumption. Therefore the focus of the work in Part II is that of identifying the underlying statistics of real HF noise, that is, the shape of the probability density function of the vertical component of the electric field of HF noise measured by a receiving system.

To begin, Chapter 4 briefly reviews the nature of the HF propagation medium, and discusses some of the HF radio-communications research (over the past 100 years) related to the study of HF noises. Though not exhaustive, the review does bring forward various definitions of HF noise. Indeed, the chapter proposes a particular definition that is fundamental to the analysis in succeeding chapters; that being that HF noise is primarily of natural origins—it is therefore impulsive—and excludes man-made (*i.e.* environmental) noise sources. This statement is not in ignorance of other definitions that include environmental noise, but is rather made with the understanding that other components, other than natural noise sources, can contribute to the statistics of HF noise depending on the location, time-of-day, and season in which the noise is measured. In the absence of other man-made components, which could be and are considered to be in this work not natural, the natural HF noise is impulsive and non-Gaussian. Work by various researchers (Clarke 1962, Ibukun 1964, Ibukun 1966, Giesbrecht *et al* 2006) support this view. The chapter concludes that a wholistic view of HF noise (one which includes man-made noise) contains a Gaussian component with narrowband interference, as well as an impulsive component largely due to lightning. This wholistic view is supported by yet others (Lemmon & Behm 1991).

With a background in place, Chapter 5 describes two methods of measuring the probability density function of HF noise: the swept-narrowband method, and the broadband method. Each method is constrained by the form of the data provided by the measuring equipment and less so from inherent limitations of the receiving equipment. The methods, designed after collection of the source data, are therefore not improvements of or replacements for methods designed by other researchers. The premise for each method is that during the sunrise period, the HF noise is dominated by galactic and

atmospheric noise. During this period, a weak environmental noise component also exists that is primarily composed of man-made signals from distant and local sources. Justification is found in the fact that during sunrise, the D-region is not yet fully formed and human activity is still at a minimum. Atmospheric noise from distant locations is therefore able to propagate to the receive site, and only weak man-made noise (both long-range and short-range) contaminates the noise statistics.

It is on this basis, that both methods excise environmental noise from the data set and generate a noise PDF from the residue. The swept-narrowband method requires data recorded from a receiver sweeping in the frequency domain, whereas the broadband method requires data recorded from a receiver that stares at a wide band for the entire measurement period. In both cases, signals with an amplitude above a threshold are removed from the data set. All data samples below the threshold are assumed to be noise samples. The HF noise PDF is generated from these noise samples using simple histogram techniques.

Chapter 6 describes the setup of receiving equipment required for measuring the HF noise distribution. Two different setups are used: one a narrowband receiver and the other a multi-antenna broadband receiver. The two receivers have some common components but do not process HF signals in the same way. The narrowband receiver (bandwidth of approximately 4 kHz) is swept in time and frequency whereas the broadband receiver, used for data collection, stares at a specific 153.6 kHz bandwidth in the HF band. The narrowband receiver was developed and used to collect data by Brine *et al* (2002) as part of a pre-emptive null-steering ionosonde. The broadband receiver was developed and manufactured by Ebor Computing.

It is important to note that the swept-narrowband method is applied to data produced from the narrowband receiver located at an urban industrial site in Adelaide, Australia. The broadband method is applied to data output from the broadband receiver, which is located at a receive site in a remote country area near Swan Reach, South Australia. With that in mind, Chapter 7 presents the results of the swept-narrowband method and broadband method.

Results of the swept-narrowband method show that the data set from Adelaide is affected by local man-made interference. Local interference (*i.e.* environmental noise)

varies from weak at dawn to strong throughout the daylight working hours. This variation is primarily due to and coincides with human activity throughout the working day. In addition, during the day, the D-region attenuates much HF noise from distant locations. Hence, there is a Gaussian component to the noise PDF, at times dominant, in addition to the natural HF noise component that is impulsive. The results of the Swan Reach measurements (using the broadband method) show no apparent strong Gaussian noise, rather they clearly show the impulsive nature of HF noise. This lack of a strong Gaussian component suggests two things: 1) the site near Swan Reach is quiet in a electromagnetic sense; and 2) the receiving system is externally noise limited at that site.

For both methods, the results indicate that the PDF of HF noise is generally not Gaussian. It appears to follow a Bi-Kappa or similar distribution, which is peaked and impulsive. Moreover, the PDF has diurnal variations and is affected by man-made groundwave and skywave interference. Significant man-made interference tends to add a Gaussian component to the PDF. This Gaussian component is strong in urban areas and weaker in remote country locations.

Chapter 7 also discusses the fitting of a modified Bi-Kappa distribution to the observed distributions, with supporting evidence provided by Clarke (1962), Ibukun (1964, 1966), and Johnson *et al* (1997). The tuning parameter, $\kappa$, of the distribution can be used to model the effect of man-made noise as well as natural HF noise. As $\kappa \rightarrow \pm\infty$ the distribution converges on a Gaussian indicating a strong man-made noise component. For $\kappa \ll \infty$, the distribution is impulsive with long tails.

Furthermore, support for the swept-narrowband method and broadband method is achieved by comparing the measured average noise levels with noise levels measured by Ebor Computing and those predicted by the ITU (CCIR 1986). The measured noise levels are generally within 10 dB of ITU predicted levels and Ebor Computing's measurements.

The chapter also proposes a technique to assess whether or not a receiving system is externally noise limited. This technique is based on the shape of the noise PDF as measured by a receiver under test. If the noise PDF has a strong Gaussian component it implies that either the receiver is not externally noise limited or the level of man-made noise at the receive site is high. If the PDF is generated from data collected by

a receiving system at a known "quiet" site and the PDF has a Gaussian component, it very likely means that the receiving system, as configured during the test, is not externally noise limited across its entire receive bandwidth.

So, with a simple empirical method it is shown that the probability density function of HF noise is not necessarily Gaussian and, in fact, depends on geographic location, time of day, and surroundings (among other things). Just before dawn HF noise is dominated by atmospheric noise propagating via skywaves. Shortly after dawn the skywave component of HF noise is much weaker, due to the absorptive properties of the D-region, and therefore local noise propagating by groundwaves becomes the dominant component. A Gaussian distribution is sufficient for development of preliminary models and algorithms, but progression to a more accurate distribution is necessary before making conclusions about the behavior of such models and algorithms.

The experiments, their results, and discussions by no means exhaust the possibilities for study of HF noise. There are many questions to be answered; some raised by other researchers and some raised by this work. For example, the HF noise PDF appears to follow a Bi-Kappa distribution. Is this generally true or is it a product of the time and location at which it was measured? In other words, how do the statistics of the HF noise vary? Are they stationary over long periods of time? Do they change with geography? What are the shapes of the PDFs generated by other measurement techniques? Do they validate the results of the swept-narrowband method and broadband method?

More information can be gleaned from the Adelaide noise data set and Swan Reach noise data set. Only the pre-dawn and post-dawn records of the Adelaide data set and Swan Reach data set have been analyzed because it is during this period of the day that the natural HF noise is best measured. However, it is well worth processing the entire data set to observe the behaviour of the HF noise over a longer period. Such a study would provide a better understanding of the diurnal changes of natural and man-made HF noise. Furthermore, both data sets warrant further analysis with other noise measurement methods, the results of which should support the results presented in this book. The other methods could employ direction-finding and null-steering to excise environmental signals and retain a truer picture of the natural HF noise. The swept-narrowband method and broadband method are, in comparison, indiscriminate

in their exclusion of assumed environmental noise sources. It is entirely possible that some of the excluded signals are actually atmospheric noise sources (*e.g.* distant lightning activity).

Finally, the outcomes of this noise study may be very useful in the design of HF receivers. Exploiting the possibility of using the HF noise PDF in specifying the characteristics of an HF receiver would be very interesting. A peaked impulsive PDF suggests that the environment is quiet and/or the HF receiver is externally noise limited. Whereas a Gaussian PDF suggests that the environment contains much interference and/or the the HF receiver is internally noise limited. The next steps are obvious: validate the previously described measurement methods; compare the Bi-Kappa distribution with the noise PDFs from an externally noise-limited receiver and the receiver under test.

On a grand scale, a global program is needed to measure the characteristics of HF noise, and indeed the HF channel, using wideband receivers. This is a point that many advocate (Watterson & Coon 1969, Watterson *et al* 1970, Vogler & Hoffmeyer 1988, Vogler & Hoffmeyer 1990, Vogler & Hoffmeyer 1992, Lemmon & Behm 1991, Lemmon & Behm 1993) but, the existence of such a program is not apparent in the literature. It is hoped that this work contributes to the understanding of the nature of HF noise and that it encourages others to continue the study of the HF environment.

Let us now leave the topic of HF noise and concentrate the remaining effort on modulation recognition issues. In particular, features that may be useful for identifying HF signals. The next part of the thesis attempts to answer the question: what parameters and features are uniquely associated with a particular modulation?